The Astrophysical Journal, 955:116 (18pp), 2023 October 1 https://doi.org/10.3847/1538-4357/aced4a

A Reanalysis of the Isolated Black Hole Candidate OGLE-2011-BLG-0462/MOA-2011-BLG-191

Casey Y. Lam and Jessica R. Lu
University of California, Berkeley, Department of Astronomy, Berkeley, CA 94720, USA; clam@carnegiescience.edu
Received 2023 May 30; revised 2023 July 31; accepted 2023 August 2; published 2023 September 25

Abstract

There are expected to be $\sim 10^8$ isolated black holes (BHs) in the Milky Way. OGLE-2011-BLG-0462/MOA-2011-BLG-191 (OB110462) is the only such BH with a mass measurement to date. However, its mass is disputed: Lam et al. measured a lower mass of 1.6–4.4 $M_\odot$, while Sahu et al. and Mróz et al. measured a higher mass of 5.8–8.7 $M_\odot$. We reanalyze OB110462, including new data from the Hubble Space Telescope (HST) and rereduced Optical Gravitational Lensing Experiment (OGLE) photometry. We also rereduce and reanalyze the HST data set with newly available software. We find significantly different ($\sim$1 mas) HST astrometry than Lam et al. in the unmagnified epochs due to the amount of positional bias induced by a bright star $\sim 0\farcs4$ from OB110462. After modeling the updated photometric and astrometric data sets, we find the lens of OB110462 is a $6.0^{+1.2}_{1.0} M_\odot$ BH. Future observations with the Nancy Grace Roman Space Telescope, which will have an astrometric precision comparable or better to HST but a field of view 100× larger, will be able to measure hundreds of isolated BH masses via microlensing. This will enable the measurement of the BH mass distribution and improve understanding of massive stellar evolution and BH formation channels.

Unified Astronomy Thesaurus concepts: Gravitational microlensing (672); Astrometric microlensing effect (2140); Stellar mass black holes (1611); Hubble Space Telescope (761)

1. Introduction

Although massive stars, the progenitors of black holes (BHs), are typically born in binaries, the majority of the Milky Way's 10^7–10^9 BHs are expected to be isolated (Fender et al. 2013; Wiktorowicz et al. 2019; Olejak et al. 2020). Around 20%–30% of O stars are expected to merge and form a single, even more massive star (Sana et al. 2012), and many of the remaining binary systems are disrupted before, during, or after the formation of the BH due to natal kicks or mass loss. Despite this, nearly all known Galactic BHs are in binary systems (Corral-Santana et al. 2016; Thompson et al. 2019; Chakrabarti et al. 2023; El-Badry et al. 2023a, 2023b). This detection bias exists because, unlike BH binaries, isolated BHs do not have a companion that can electromagnetically identify their presence, making them particularly elusive. Detecting and characterizing isolated BHs is a critical first step needed to understand the full Galactic BH population.

Gravitational lensing is the most practical way to detect isolated BHs, as the observational signature depends only on the mass of the lens, and not its luminosity. In particular, microlensing, the regime of gravitational lensing where the images are unresolved, provides a way to find and measure the masses of dark objects. As a foreground lens (e.g., a BH) aligns in front of a background source of light (e.g., a Bulge star), this causes the background source to brighten temporarily and change its apparent position; the transient brightening is called photometric microlensing and the transient change in position is called astrometric microlensing. The combination of the photometric and astrometric signals can be used to measure the mass, distance, and proper motion of the lens (Hog et al. 1995; Miyamoto & Yoshii 1995; Walker 1995). For more details on astrometric microlensing, see Dominik & Sahu (2000).

1.1. An Isolated Dark Compact Object Found with Microlensing

OGLE-2011-BLG-0462/MOA-2011-BLG-191 (hereafter OB110462) is the first isolated, dark compact object to have its mass measured with astrometric microlensing. It was identified as a microlensing event toward the Galactic Bulge located at (17:51:40.19, −29:53:26.3) and has been observed both photometrically and astrometrically in order to measure the lens' mass. However, the nature of OB110462's lens is disputed. Sahu et al. (2022) inferred the lens to be a $M_L = 7.1 \pm 1.3\ M_\odot$ dark object, making OB110462 a firm BH detection similar in mass to other known Galactic BHs in binary systems. Lam et al. (2022a, 2022b) inferred a lower mass object, which depending on the modeling, led to a $M_L = 2.15^{+0.67}_{-0.54} M_\odot$ or $M_L = 3.79^{+0.62}_{-0.57} M_\odot$ dark object, implying a neutron star or low-mass BH. Both groups analyzed slightly different subsets of high-cadence ground-based photometry and high-resolution Hubble Space Telescope (HST) astrometry; see Mróz et al. (2022) for a summary. In particular, despite analyzing the same astrometric data, both groups derived different stellar positions. In addition, they both found that the microlensing parameters inferred from the ground-based photometry were in tension with the parameters inferred by their respective astrometric measurements.

Mróz et al. (2022) reanalyzed the ground-based Optical Gravitational Lensing Experiment (OGLE) photometry of OB110462. They found systematics in the photometry resulting from imperfect image subtraction due to variations in seeing. Updated modeling using the revised data showed that the OGLE photometry could be self-consistently modeled with the astrometry of Sahu et al. (2022), and Mróz et al. (2022) inferred a lens mass of $M_L = 7.88 \pm 0.82\ M_\odot$.

Mereghetti et al. (2022) combined new and archival Chandra imaging to search for X-ray emission from OB110462. No X-rays were detected, and based on the detection upper limits, concluded OB110462 could be consistent with an accreting isolated BH with low radiative efficiency. A neutron star moving slowly or in a high-density environment would be disfavored, but uncertainties in the velocity and environment density, as well as the accretion efficiency, did not allow stronger statements to be made on the nature of OB110462.

1.2. Rationale for Reanalysis of OB110462

Since publication of the initial discovery and modeling papers of OB110462 in 2022 July, there have been several new developments. First, as mentioned in Section 1.1, there are updated ground-based photometry data from OGLE. There are also two additional HST data points for OB110462. OB110462 was one of 70 targets in a HST snapshot program to image microlensing events (SNAP-16716; PI: K. Sahu); observations of OB110462 were taken in 2022 May. In addition, the second and final epoch of a Cycle 29 program (GO-16760; PI: C. Lam) to obtain OB110462 astrometry was taken in 2022 September. With regards to analysis tools, an updated version of the software used in the extraction of the astrometry from the HST data (`hst1pass`; Anderson 2022) was released in 2022 July.

The ability to find and characterize isolated BHs is necessary to understand the evolution and death of massive stars. In turn, massive stars impact our understanding of a wide range of astrophysical problems, from the high-mass end of the stellar initial mass function, to chemical evolution, to galactic feedback. Without understanding the properties of isolated BHs, these problems cannot be solved. Thus, a reanalysis of OB110462 is a timely and worthwhile pursuit.

The remainder of this paper is outlined as follows. Section 2 lists the new and updated data used in this reanalysis of OB110462. Section 3 describes the new and updated capabilities of the `hst1pass` software and their effect on the measurements of source positions and magnitudes. Section 4 describes how these updated measurements are used to derive an updated astrometric time series, and Section 5 describes how both the updated photometry and astrometry are fit with a microlensing model. Section 6 presents the lens' properties, compares them to previous studies of OB110462, and shows that the choice of software significantly affects the astrometry and in turn the lens mass. Section 7 discusses OB110462 in the context of the known Galactic BH population and considers future searches for BHs. Section 8 provides a summary and conclusions.

2. Observations

2.1. HST

Eleven epochs of HST observations of OB110462 were obtained between 2011 and 2022, and are presented in Table 1. This includes all the data analyzed in Lam et al. (2022a, 2022b; see Table 2 in Lam et al. 2022b), with several additions. First, all exposures taken on 2011 August 8 were included in this analysis (compared to Lam et al. 2022a, 2022b, who excluded three frames that had different exposure times than the main data set). The exposures from 2013 May 13 were also included (compared to Lam et al. 2022a, 2022b, who excluded them because there were no other spring epochs to calibrate them, resulting in reference frame alignment issues due to parallax; however there is now a second spring epoch that can be used to perform this calibration). Finally, the new HST observations taken in 2022 have been included. Note that although the 2022 September 13 GO data were taken with the UVIS2-2K2C-SUB subarray like the previous data sets, the 2022 May 29 SNAP data were taken with the UVIS2-C1K1C-SUB subarray, which is a smaller subarray (1k × 1k, versus 2k × 2k).

Table 1
HST Data Analyzed

Epoch (UT)	PA (deg)	Filter	$T_{\rm exp}$ (s)	$N_{\rm im}$
2011-08-08	270.0	F606W	75.0	3
2011-08-08	270.0	F606W	60.0	1
2011-08-08	270.0	F814W	75.0	3
2011-08-08	270.0	F814W	60.0	1
2011-08-08	270.0	F814W	120.0	1
2011-10-31	276.1	F606W	280.0	3
2011-10-31	276.1	F814W	200.0	4
2012-09-09	269.5	F606W	290.0	3
2012-09-09	269.5	F814W	190.0	4
2012-09-25	271.3	F606W	280.0	3
2012-09-25	271.3	F814W	200.0	4
2013-05-13	99.9	F606W	280.0	3
2013-05-13	99.9	F814W	200.0	4
2013-10-22	274.6	F606W	285.0	3
2013-10-22	274.6	F814W	285.0	4
2014-10-26	275.2	F606W	265.0	3
2014-10-26	275.2	F814W	265.0	4
2017-08-29	268.3	F606W	250.0	3
2017-08-29	268.3	F814W	250.0	4
2021-10-01	272.0	F606W	407.0	5
2021-10-01	272.0	F814W	307.0	6
2022-05-29	107.9	F814W	300.0	2
2022-09-13	269.9	F606W	407.0	5
2022-09-13	269.9	F814W	307.0	6

Note. HST data. For each epoch, the position angle (PA), HST WFC3/UVIS filter, exposure time $T_{\rm exp}$, and number of images $N_{\rm im}$ are listed. Bold text indicates data used in this reanalysis that were not used in Lam et al. (2022a, 2022b).

2.2. OGLE

As mentioned in Section 1, the ground-based OGLE photometry was rereduced by Mróz et al. (2022). Figure 1 shows the difference between the old and new light curves. In addition, Mróz et al. (2022) found that data from the first half of 2010 were affected by systematics due to commissioning of a new camera, and removed these data from their analysis. They also only modeled data through 2016 as they found a potential systematic in old OGLE reductions around HJD = 2,458,000 (2017 September). For consistency, we also model the same subset of rereduced OGLE data, spanning HJD = 2,455,376–2,457,700 (roughly 2010 July–2016 November).

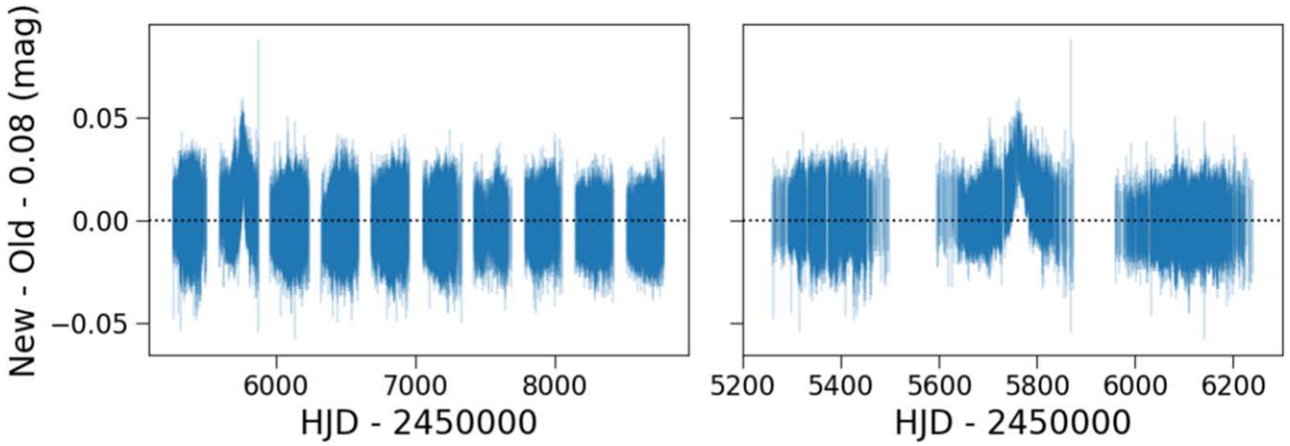

Figure 1. Difference between the OGLE photometry used in Mróz et al. (2022) to that used in Lam et al. (2022a, 2022b) and Sahu et al. (2022). Left: full light curve. Right: light curve zoomed into the first three years (photometric peak year ±1 yr).

3. Updated Astrometric Reductions and Analysis with `hst1pass`

The software package `hst1pass` extracts precise astrometry from HST WFC3/UVIS imaging. It is described in Anderson & King (2006), and although it has been updated and used in many publications over the years, it was never formally released as Space Telescope Science Institute–supported software. Lam et al. (2022a, 2022b) and Sahu et al. (2022) used one of these unofficial `hst1pass` releases to perform their astrometric analyses.

In 2022 July `hst1pass` was officially released (Anderson 2022). Most notably, this release included a tabular correction for charge transfer efficiency (CTE; Anderson 2021) that could be used instead of a pixel-based CTE correction (Anderson et al. 2021), and new functionality to perform artificial star injection-and-recovery simulations.

We note that the official release of `hst1pass` also comes with a new routine called `hst2collate` to collate starlists of the individual frames together into a final starlist for that epoch. However, because this is a limited-use early version of `hst2collate`, we find the flexibility of the existing software routines `xym2mat` and `xym2bar` (Anderson & King 2006) to be superior. Hence, we do not use `hst2collate` in our analysis and do not discuss it further here.

3.1. CTE Correction

Lam et al. (2022a, 2022b) and Sahu et al. (2022) used CTE-corrected flat-fielded HST images (i.e., `flc`) for their analyses. The `flc` images were produced using version 2.0 of a pixel-based CTE-correction algorithm (Anderson et al. 2021). However, the pixel-based correction usually undercorrects the CTE effect on photometry (Kuhn & Anderson 2021).

The updated version of `hst1pass` includes a tabular correction that empirically corrects for CTE based on the brightness of the source and the sky background, which improves the extraction of photometry and astrometry (Anderson 2021).

Both CTE-correction methods alter the extracted source positions in the detector *y*-direction, which is the parallel readout direction. At present, CTE in the detector *x*-direction, which is the serial readout direction, is not corrected. Although there is CTE in the serial readout direction, it is negligibly small compared to the CTE in the parallel readout direction (Anderson 2014).

When performing the data reduction in this work, instead of reducing the CTE pixel-corrected `flc` files, we instead reduce the flat-fielded data files (i.e., `flt`) with `hst1pass` using the tabular CTE corrections Measured positions between these two methods can differ by a tenth of a pixel and the measured brightnesses can differ by a tenth of a magnitude (Figure 16 in Appendix A). We then proceed with the data reduction and intraepoch alignment process described in Section 4.1 of Lam et al. (2022b) using the tabular-CTE-corrected starlists.

3.2. Artificial Star Injection-and-recovery Tests

OB110462 is located ∼10 pixels (∼0.″4) away from an unrelated neighbor star that is 3 magnitudes brighter. This neighbor star biases the measurement of the flux and position of OB110462. Lam et al. (2022a, 2022b) and Sahu et al. (2022) took different approaches to calculate this bias.

Sahu et al. (2022) used 18 nearby isolated stars with colors and magnitudes comparable to the neighbor to construct an "extended model" point-spread function (PSF). This extended model PSF was then subtracted from each exposure to obtain an unbiased position and magnitude of OB110462. Using this method, Sahu et al. (2022) found that the typical positional bias for OB110462 was about 1.2 mas.

Lam et al. (2022a, 2022b) performed injection-and-recovery tests to measure the bias. They injected sources around an isolated star of similar brightnesses to the neighbor, at the same azimuth, separation, and magnitude difference as the neighbor–OB110462 pair. Using this method, Lam et al. (2022b) found a smaller positional bias of around 0.3 and 0.5 mas for OB110462, in the F606W and F814W filters, respectively.

In Section 3.2.1 we describe the new `hst1pass` software used to perform source extraction for artificial stars and in Section 3.2.2, we present an updated and more extensive star-planting analysis using the new `hst1pass`.

3.2.1. `hst1pass` Versus `ks2` Software

The version of `hst1pass` used by Lam et al. (2022a, 2022b) did not have a method to generate artificial stars in the images. Thus, Lam et al. (2022a, 2022b) used a different software package, called `ks2`, to perform the injection-and-recovery tests. `ks2` has not been formally

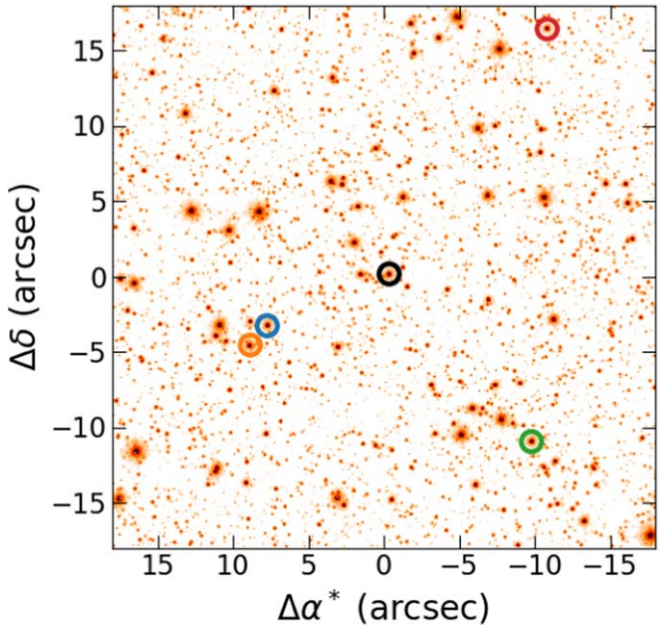

Figure 2. Spatial distribution of neighbor-like stars. The image shows a $36'' \times 36''$ area centered on OB110462. The black circle in the center shows the location of OB110462's bright neighbor. The four other colored circles show the location of the neighbor-like stars.

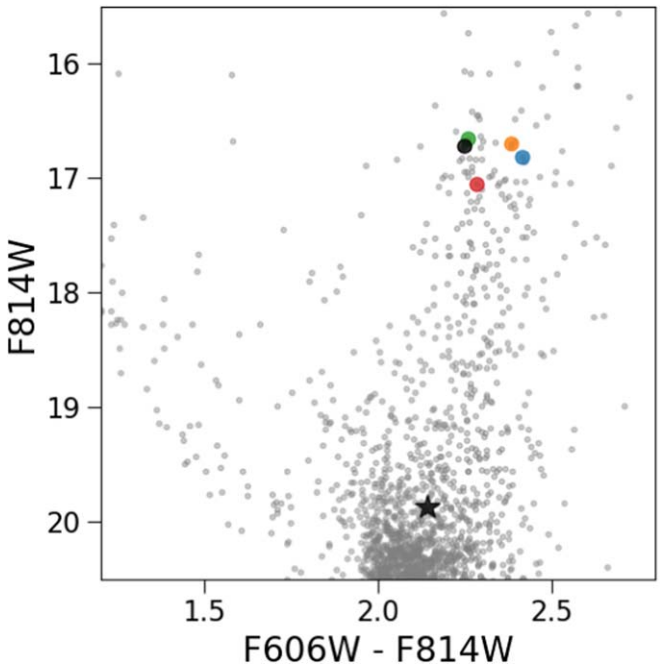

Figure 3. Location of neighbor-like stars on an HST CMD. The black circle marks OB110462's bright neighbor. The four other colored circles mark the neighbor-like stars (colors correspond to those in Figure 2). The black star marks OB110462 at baseline (i.e., unmagnified).

released, but it is described in several papers, e.g., Anderson et al. (2008), Sabbi et al. (2016), and Bellini et al. (2018).

Although both `hst1pass` and `ks2` are used to extract precise astrometric measurements from HST imaging, they work in slightly different manners. `ks2` was specifically designed to find fainter sources than `hst1pass`. There are also certain implementation differences across the two software packages. Of relevance to the astrometry are the geometric distortion solutions used, and the specifics of the PSF fitting. With regard to the distortion solution, `ks2` has an internal geometric distortion solution that is slightly different from the standard geometric distortion correction (STDGDC) files used by `hst1pass`. With regard to the PSFs, the specific manner of fitting slightly differ, e.g., the particulars of how outlier rejection is implemented.

In Lam et al. (2022a, 2022b), `hst1pass` was used instead of `ks2` for data reduction because recovery depth was not an issue and `hst1pass` had been more robustly used and tested on HST WFC3/UVIS data. To use `hst1pass` to obtain the positions, and then use `ks2` to calculate the bias in the position and flux of OB110462 is formally inconsistent, since the two methods of source extraction in these software differ. As a validation test, `hst1pass` and `ks2` were used to extract astrometry from the same epoch of HST observations and then the differences between the resultant starlists were compared. No clear trends were found to explain the differences. Since the bias correction is a relative measurement and self-consistent across one software package, it was deemed a reasonable approach to calculate the bias correction with `ks2` and then apply it to measurements made with `hst1pass`. However, now that the new version of `hst1pass` has the ability to simulate artificial stars, the injection-and-recovery analysis can be done in a fully self-consistent manner and this assumption can be checked.

3.2.2. Updated Methodology

Here, we update the analysis performed in Lam et al. (2022b). We briefly summarize the methodology here and only highlight new changes; see Appendix B of Lam et al. (2022b) for full details.

We calculate the bias in the position and flux of OB110462 by injecting artificial stars using `hst1pass` at the same azimuth and separation as OB110462 and its bright neighbor star, around "neighbor-like" stars. We then determine whether these injected artificial stars are recovered, and if they are, how different the recovered and injected positions and fluxes are.

The criteria for selecting nearby isolated neighbor-like stars are:

1. similar brightness to neighbor (within ± 0.5 mag in both F814W and F606),
2. similar color to neighbor (within ± 0.25 mag in F606W–F814W),
3. nearby to neighbor (within $\pm 20'' = 500$ pixels)
4. isolated from other stars (at least $0\farcs4 = 10$ pixels away from any other source detected by `hst1pass` in F814W).

There are four stars that fit all these criteria. Their positions in relation to OB110462 are shown in Figure 2 and on a color–magnitude diagram (CMD) in Figure 3.

Forty-five artificial stars are injected in a 0.2×0.2 pixel ($=8 \times 8$ mas) area adjacent to each of the four neighbor-like stars, with a magnitude so that the artificial star has the same contrast with the neighbor-like star as OB110462 to its neighbor. The results of the injection and recovery are shown in Figures 4 and 12 (see Figures 22 and 23 in Lam et al. 2022b) and listed in Table 2 (see Table 16 in Lam et al. 2022b).

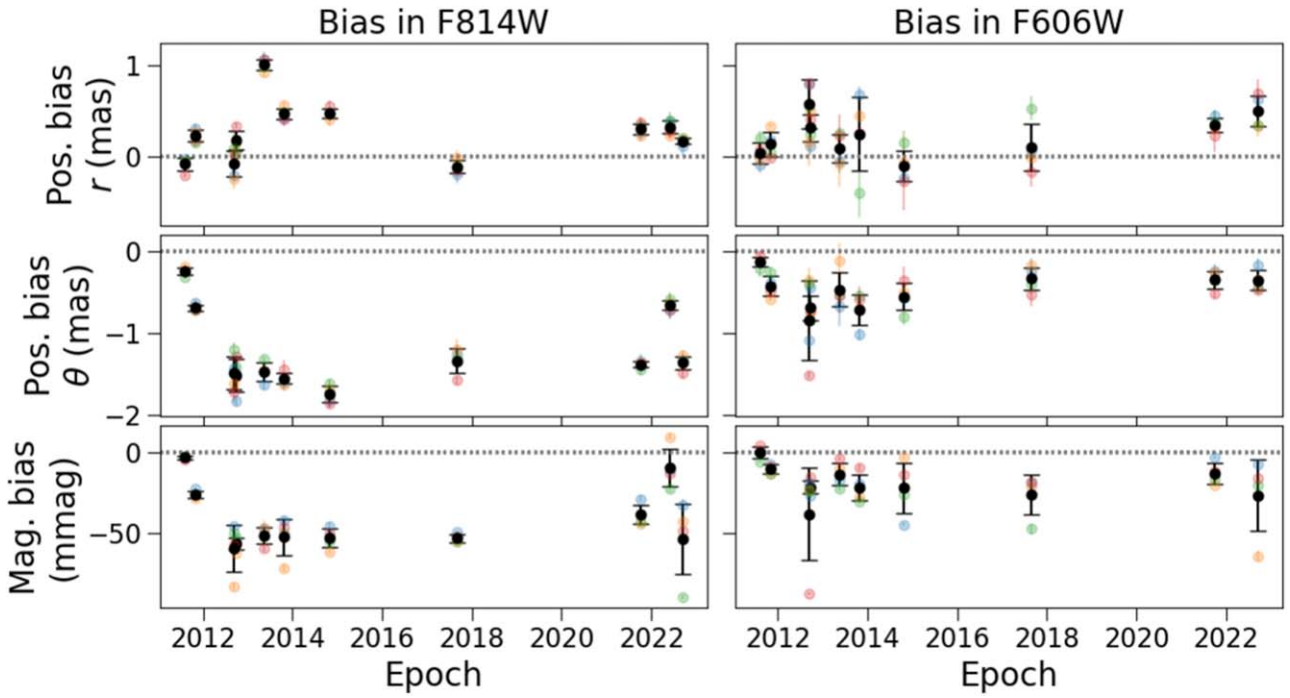

Figure 4. Measurement bias of a source in F814W (left) and F606W (right) due to proximity to a bright star. The bias correction is defined as the recovered minus injected value. The amount of positional bias is shown decomposed into radial r (top row) and azimuthal θ (middle row) components. The radial direction is defined by the OB110462-neighbor star separation vector, and the azimuthal direction is measured counterclockwise from the separation vector. The amount of magnitude bias is shown in the bottom row. The colored points show the mean and standard deviation of the measurement bias for the four different neighbor-like stars; the colors correspond to those in Figures 2 and 3. The black points are the mean and standard deviation of the mean measurement bias of the four neighbor-like stars. The positional and magnitude bias in F606W is smaller than that in F814W by about a factor of two; this is not surprising since at shorter wavelengths the angular resolution is higher.

Table 2
Bias Correction Derived from Injection and Recovery

Epoch	ΔR.A. (mas)	ΔDecl. (mas)	ΔTotal (mas)	ΔMag (mag)
F606W				
2011-08-08	-0.14 ± 0.08	0.00 ± 0.10	0.14	0.000 ± 0.004
2011-10-31	-0.46 ± 0.14	0.00 ± 0.11	0.46	-0.010 ± 0.003
2012-09-09	-0.98 ± 0.53	-0.27 ± 0.15	1.02	-0.039 ± 0.029
2012-09-25	-0.76 ± 0.17	-0.08 ± 0.12	0.76	-0.022 ± 0.004
2013-05-13	-0.48 ± 0.22	0.06 ± 0.13	0.48	-0.013 ± 0.007
2013-10-22	-0.76 ± 0.29	-0.01 ± 0.33	0.76	-0.022 ± 0.008
2014-10-26	-0.50 ± 0.20	0.27 ± 0.12	0.57	-0.022 ± 0.016
2017-08-29	-0.36 ± 0.15	0.00 ± 0.25	0.36	-0.026 ± 0.012
2021-10-01	-0.44 ± 0.08	-0.22 ± 0.10	0.49	-0.013 ± 0.007
2022-09-13	-0.50 ± 0.12	-0.36 ± 0.16	0.62	-0.027 ± 0.022
F814W				
2011-08-08	-0.21 ± 0.05	0.15 ± 0.07	0.26	-0.003 ± 0.001
2011-10-31	-0.73 ± 0.02	0.00 ± 0.07	0.73	-0.026 ± 0.002
2012-09-09	-1.39 ± 0.18	0.55 ± 0.17	1.49	-0.060 ± 0.015
2012-09-25	-1.50 ± 0.18	0.31 ± 0.13	1.53	-0.057 ± 0.003
2013-05-13	-1.72 ± 0.12	-0.47 ± 0.05	1.78	-0.052 ± 0.005
2013-10-22	-1.63 ± 0.08	0.05 ± 0.05	1.63	-0.053 ± 0.012
2014-10-26	-1.81 ± 0.10	0.11 ± 0.03	1.81	-0.053 ± 0.006
2017-08-29	-1.23 ± 0.13	0.53 ± 0.10	1.34	-0.053 ± 0.002
2021-10-01	-1.41 ± 0.05	0.15 ± 0.05	1.42	-0.039 ± 0.006
2022-05-29	-0.74 ± 0.06	-0.10 ± 0.07	0.74	-0.009 ± 0.012
2022-09-13	-1.35 ± 0.07	0.27 ± 0.04	1.37	-0.054 ± 0.022

Note. Bias correction derived from injection/recovery around a star of comparable brightness at the same separation, azimuth, and magnitude difference as OB110462 to its bright neighbor. The bias correction is defined as the recovered minus the true injected value.

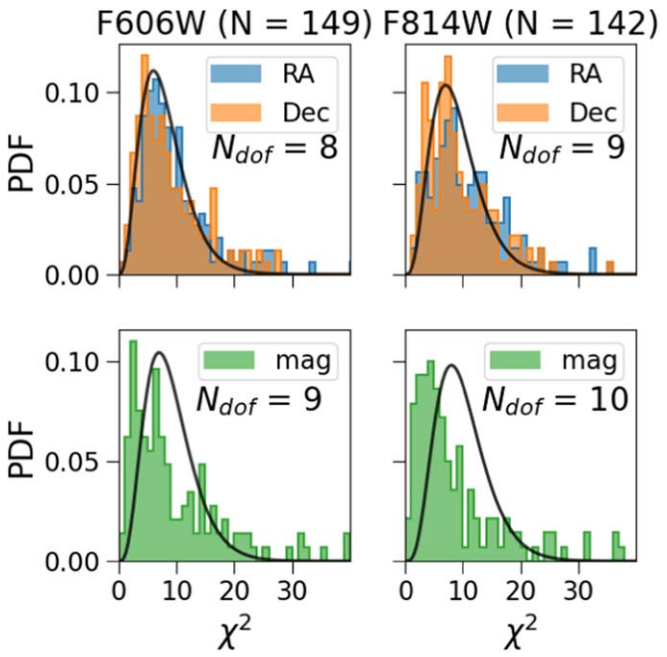

Figure 5. Top: histograms of χ^2 residual values to linear proper motion fits (no parallax) of the reference stars. Bottom: histograms of χ^2 residual values to constant magnitude vs. time fits of the reference stars. The left column shows the reference stars for F606W; the right column shows the reference stars for F814W. *N* denotes the number of reference stars.

4. Updated Cross-epoch Alignment

We take the starlists for epoch obtained in Section 3.1 and align them onto a common reference frame, as described in Sections 4.2–4.2.3 of Lam et al. (2022b). The photometry is calibrated as described in Section 4.3 of Lam et al. (2022b); in short, to obtain precise relative photometry, we calculate and apply a small magnitude offset that assumes the reference stars have constant brightness. One minor change in this work as compared to Lam et al. (2022b) is the value of the additive error added in quadrature to the positional and magnitude uncertainties. Appendix A of Lam et al. (2022b) describes an empirical methodology to calculate the rescaling factor, which can vary epoch to epoch. We instead simply use a constant additive error across all epochs; the value of the additive error is chosen to make the alignment residuals follow the expected χ^2 distribution. We find an additive error of 0.25 mas and 12 mmag added to the F606W positions and magnitudes, and 0.10 mas and 8 mmag in F814W, produce acceptable χ^2 distributions by eye (Figure 5; see Figure 9 of Lam et al. 2022b.). Figures 6 and 7 show the 10 astrometric reference stars closest to OB110462.

The final result of the cross-epoch alignment is an HST photometric and astrometric time series (Figures 8 and 9). The bias correction measured in Section 3.2.2 is then applied to OB110462 to obtain its true position and magnitude (Table 3). Note that in Table 3 the reported uncertainties do not include the uncertainties in the transformation from the relative astrometric reference frame to the absolute Gaia reference frame, which are 0.13 mas yr^{-1} and 0.11 mas yr^{-1} in R.A. and decl., respectively.

5. Modeling Using the Updated Data

Next, we fit the rereduced OGLE data and updated HST data following the procedure outlined in Lam et al. (2022a, 2022b) for their "default weight" (DW) fit. See Section 5 of Lam et al. (2022b) for details on the model parameters and modeling framework.

Simultaneously fitting the photometry and astrometry is very time intensive, so to speed up the process, we first simultaneously fit the OGLE and HST photometry, accounting for correlated noise while fitting the OGLE photometry with a GP. The joint photometric and astrometric geometric parameters are t_0, u_0, t_E, $\pi_{E,E}$, and $\pi_{E,N}$. The photometric-only parameters are $b_{SFF,O}$, $m_{base,O}$, $b_{SFF,H8}$, $m_{base,H8}$, $b_{SFF,H6}$, and $m_{base,H6}$. The astrometric-only parameters are $x_{S0,E}$, $x_{S0,N}$, π_S, $\log_{10}\theta_E$, $\mu_{S,E}$, and $\mu_{S,N}$. The GP parameters are $\log\sigma_{0,O}$, ρ_O, $\log\omega_{0,O}^4 S_{0,O}$, and $\log\omega_{0,O}$. See Section 3 of Lam et al. (2022a), and Section 5, Section 5.1, and Appendix F of Lam et al. (2022b) for a full description of all these parameters.

We then take the posterior distributions for t_0, u_0, t_E, $\pi_{E,E}$, and $\pi_{E,N}$ from the photometric fit, and use them as priors when fitting the HST astrometry. Note the correlations between the five parameters are preserved when using them as priors in the astrometry fit. Our priors are listed in Table 8 in Appendix B.

6. Results

The best-fit photometric and astrometric models are shown in Figures 8 and 9, and the posteriors are listed in Table 4. We find that the lens of OB110462 has a mass of $M_L = 6.03^{+1.19}_{-1.04} M_\odot$, is at a distance of $D_L = 1.72^{+0.32}_{-0.23}$ kpc, and has a transverse velocity of $v_{T,L} = 37.61^{+5.12}_{-5.13}$ km s^{-1}.

OB110462 cannot be a high-mass star, and is thus a BH. In Lam et al. (2022a, 2022b), they rule out any possibility of a luminous lens for OB110462, for a lens mass of $M_L = 3.8\ M_\odot$ and source flux fractions of $b_{SFF} = 0.9$ and 0.94 in F814W and F606W, respectively. Here, we find $M_L = 6.0\ M_\odot$ and source flux fractions $b_{SFF} = 0.98$ in both F814W and F606W. In both Lam et al. (2022a, 2022b) and this work, the lens is $D_L = 1.7$ kpc away. In this work, the mass is significantly higher and the source flux fractions are also slightly higher. This means the constraint on a dark lens is much stronger—given the lens is at some fixed distance, a higher-mass star would be much brighter, and a higher source flux fraction would mean there is less excess flux that such a star could hide in. Thus, without any shadow of a doubt, OB110462 is a BH.

In the next sections we compare these results to those of Lam et al. (2022a, 2022b), Sahu et al. (2022), and Mróz et al. (2022). Table 5 gives a short summary of the differences in the data and models used to analyze OB110462 across these works. We first compare the inferred lens properties in Section 6.1, evaluate the goodness of fits of the astrometric models in Section 6.2, then compare the modeled astrometric time series in Section 6.3 to understand the reasons for the differences in the inferred lens properties.

6.1. Comparison of the Inferred Microlensing Parameters

We compare the inferred lens mass, distance, transverse velocity, and proper motion of OB110462 to Lam et al. (2022a, 2022b), Sahu et al. (2022), and Mróz et al. (2022) in Table 6 and Figure 10. Mróz et al. (2022) provide two sets of D_L and $v_{T,L}$ depending on the source distance assumed. The two solutions are consistent with each other to 1σ; here we only compare to their results using $D_S = 8.8 \pm 1.4$ kpc. In addition, Sahu et al. (2022) do not report their uncertainties on the lens

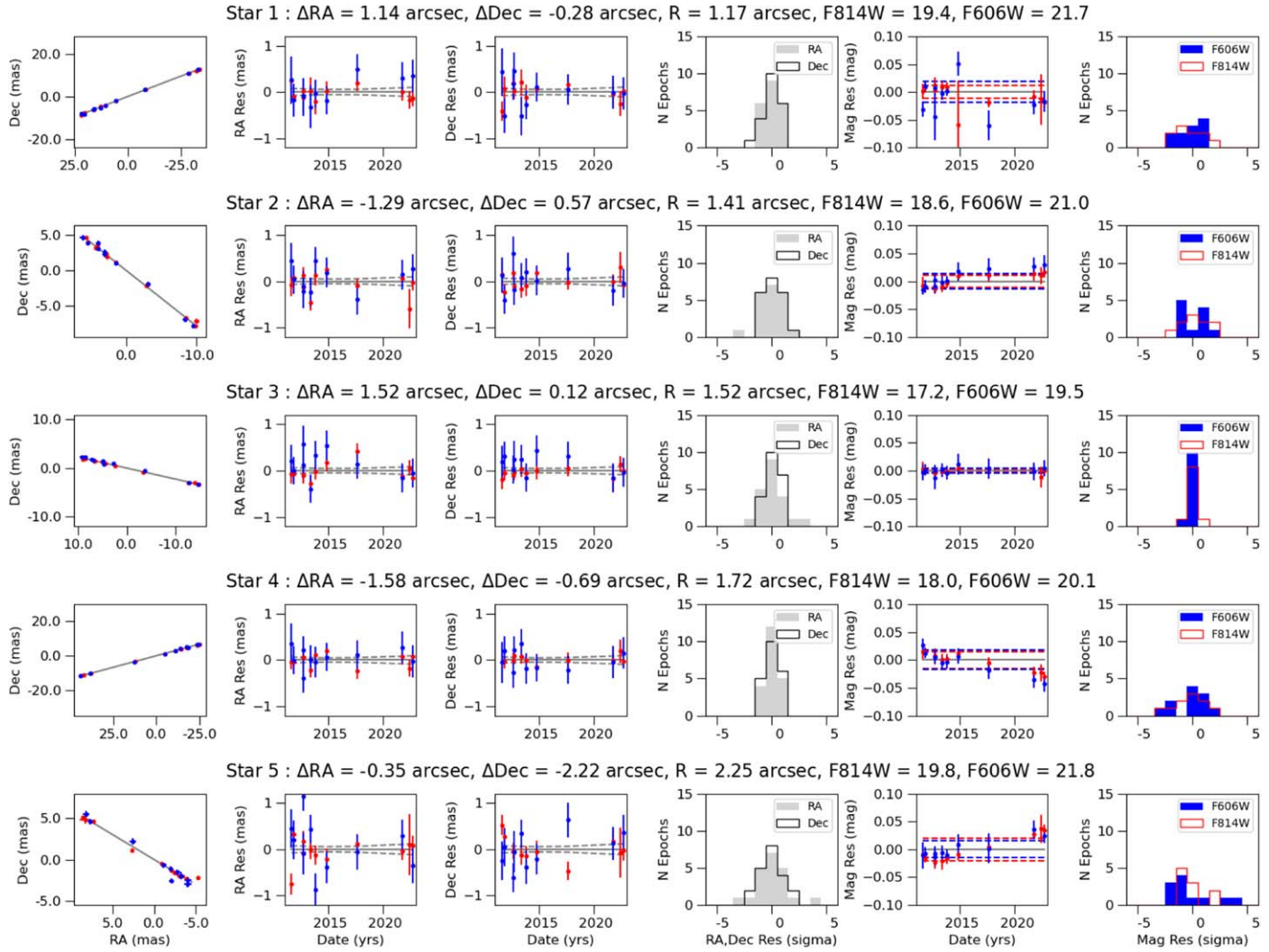

Figure 6. Five reference stars nearest to OB110462. The title indicates the separation of the reference star from OB110462 in R.A., decl., and total distance, and the magnitude of the star in F814W and F606W. In the individual panels, data in the F606W (F814W) filters are shown in blue (red). First column: trajectory on sky. Note the scales across different rows vary. The positions are relative to the ΔR.A., and Δdecl. offsets, which are relative to OB110462. The best-fit linear trajectory is shown in gray. Note these velocities are in a reference frame where the mean velocity of the reference stars is 0, and not the Gaia reference frame. Second column: residuals to the best-fit linear trajectory in R.A. The dashed lines are the 1σ uncertainties to the best-fit line. Third column: same as the second column, but for decl. instead of R.A. Fourth column: histograms of the position residuals to the best-fit linear trajectory, in units of σ. The solid gray is for R.A.; the outlined black is for decl. Fifth column: residuals to the best-fit constant magnitude. F814W and F606W are fit to the respective magnitudes in the title; the dashed lines show the 1σ uncertainties to the best-fit magnitude. Sixth column: residuals to the best-fit constant magnitude, in units of σ. The solid blue is for F606W; the outlined red is for F814W.

transverse velocity; we estimate it to be ∼5.5 km s^{-1} based on the reported lens proper motion and distance uncertainties.

The lens mass of OB110462 inferred in this work $M_L = 6.03^{+1.19}_{-1.04} M_\odot$ is consistent with the measurement of Sahu et al. (2022) $M_L = 7.1 \pm 1.3\ M_\odot$ to 1σ, and consistent with the Lam et al. (2022a, 2022b) DW model $M_L = 3.79^{+0.62}_{-0.57} M_\odot$ and Mróz et al. (2022) $M_L = 7.88 \pm 0.82\ M_\odot$ measurement to 2σ (in different directions). Our uncertainties are likely larger due to using wider priors for the astrometry; Mróz et al. (2022) state they use uniform priors in their modeling, but do not state the support.

The lens distance $D_L = 1.72^{+0.32}_{-0.23}$ kpc inferred in this work is consistent with the measurements of Lam et al. (2022a, 2022b) DW model $D_L = 1.67^{+0.26}_{-0.20}$ kpc, Sahu et al. (2022) $D_L = 1.58 \pm 0.18$ kpc, and Mróz et al. (2022) 1.62 ± 0.15 kpc to 1σ.

The lens transverse velocity $v_{T,L} = 37.61^{+5.12}_{-5.13}$ km s^{-1} inferred in this work is consistent with Mróz et al. (2022) $v_{T,L} = 43.4 \pm 3.8$ km s^{-1} and Sahu et al. (2022) $v_{T,L} \sim 45 \pm 5.5$ km s^{-1} to 1σ. It is consistent with the Lam et al. (2022a, 2022b) DW model $v_{T,L} = 23.95^{+2.95}_{-2.95}$ km s^{-1} to 2σ.

The lens proper motion $(\mu_{L,E}, \mu_{L,N}) = (-3.80^{+0.48}_{-0.55}, 2.60^{+0.83}_{-0.80})$ mas yr^{-1} inferred in this work is consistent with Mróz et al. (2022) $(\mu_{L,E}, \mu_{L,N}) = (-4.48 \pm 0.39, 3.29 \pm 0.5)$ mas yr^{-1} and Sahu et al. (2022) $(\mu_{L,E}, \mu_{L,N}) = (-4.36 \pm 0.22, 3.06 \pm 0.66)$ mas yr^{-1} to 1σ in R.A. and decl. The proper motion inferred by the Lam et al. (2022a, 2022b) DW model $(\mu_{L,E}, \mu_{L,N}) = (-2.64^{+0.18}_{-0.24}, 1.46^{+0.63}_{-0.71})$ mas yr^{-1} is discrepant to this work $\sim 3\sigma$ in R.A. and consistent to this work $\sim 2\sigma$ in decl. (the measurements in decl. have larger uncertainties than in R.A.).

The direction of the lens–source relative proper motion φ is not a property of the lens itself, but was an important point of comparison across previous work so we consider it here. It is defined in Sahu et al. (2022) as the PA of the lens–source

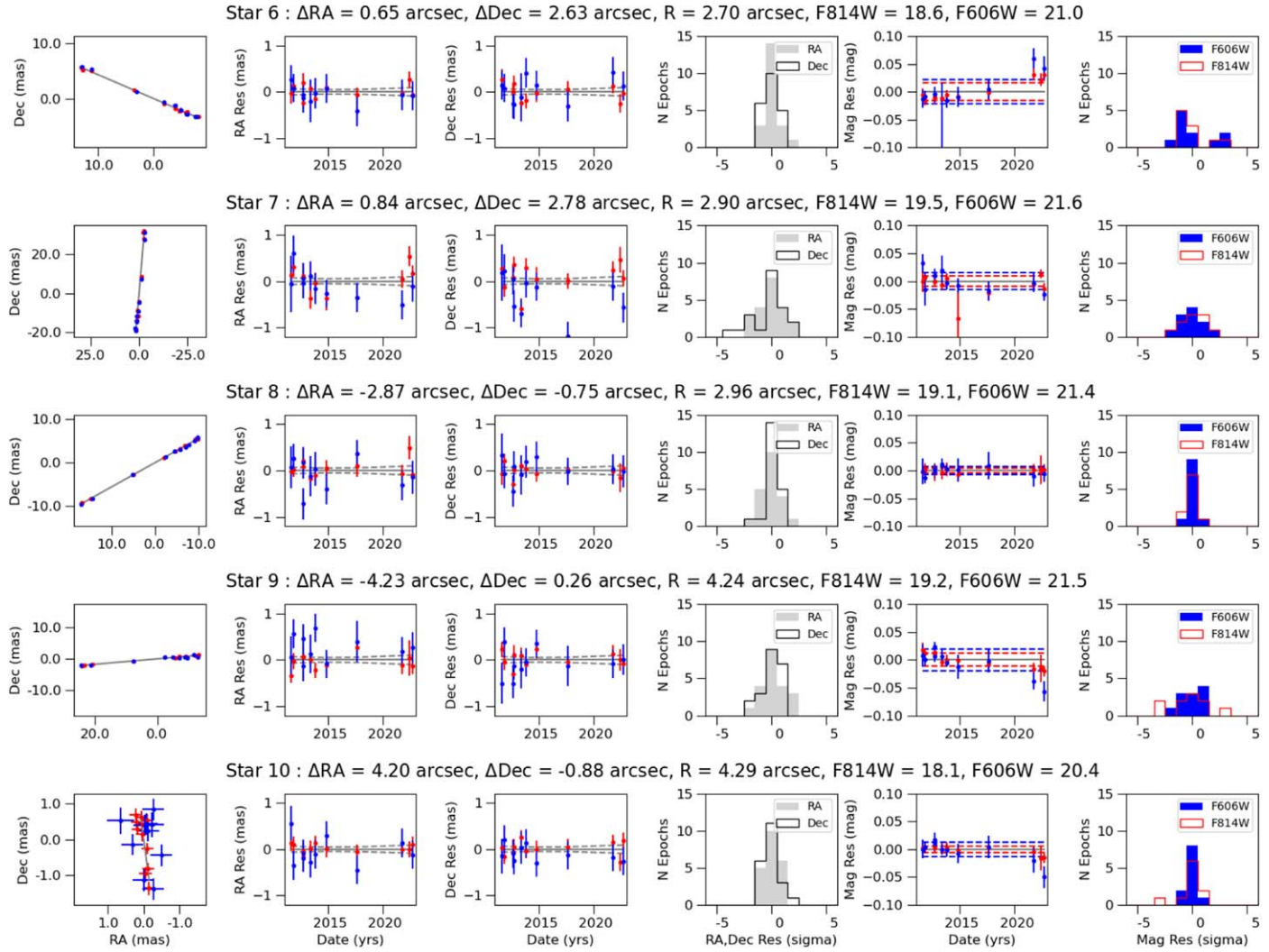

Figure 7. Same as Figure 6, but for the next five reference stars nearest to OB110462.

relative proper motion in equatorial coordinates. In this work, we find $\varphi = 343.75^{+4.80}_{-3.95}$ degrees, consistent with the measurements of Mróz et al. (2022) $\varphi = 342.5 \pm 4.9$ degrees and Sahu et al. (2022) $\varphi = 342.3 \pm 3.0$ degrees to 1σ. The value of Lam et al. (2022a, 2022b) from the DW model $\varphi = 355.47^{+2.66}_{-2.11}$ is discrepant at $>2\sigma$ from this work.

The photometric and astrometric measurements independently constrain φ. Modeling the rereduced OGLE photometry alone yields $\varphi = 345.1 \pm 3.7$ degrees (Mróz et al. 2022). Modeling the rereduced HST astrometry presented here alone measures $\varphi = 326.9^{+11.5}_{-11.0}$ degrees. The updated photometry and astrometry are consistent with each other to $<2\sigma$.

In general, the properties of the lens of OB110462 inferred in this work are somewhat discrepant with the Lam et al. (2022a, 2022b) DW model, and in reasonable agreement with Sahu et al. (2022) and Mróz et al. (2022). We also note that they are inconsistent with the Lam et al. (2022a, 2022b) EW model; the measurements of $M_L = 2.15^{+0.67}_{-0.54} M_\odot$, $D_L = 0.92^{+0.38}_{-0.22}$ kpc, $v_{T,L} = 7.26^{+4.88}_{-4.88}$ km s^{-1}, $(\mu_{L,E}, \mu_{L,N}) = (-0.69^{+0.91}_{-0.94}, 1.53^{+1.21}_{-1.12})$, and $\varphi = 18.08^{+8.60}_{-8.31}$ are discrepant by $>3\sigma$ in mass, lens–source relative proper motion, and lens proper motion in R.A. and $>4\sigma$ in transverse velocity with this work.

6.2. Goodness of Fits

Next, we consider the goodness of fits of the astrometric model to the data. As a reminder, the data and models used for each work are summarized in Table 5. Figure 11 shows the cumulative distribution function (CDF) of the normalized residuals of the astrometric data and models against the CDF of a standard normal distribution. For all the data sets except Sahu et al. (2022), the astrometry in F606W and F814W are separate data points; Sahu et al. (2022) averages astrometry across both F606W and F814W filters to obtain a single position. The residuals in this work are in good agreement with that of a standard normal, as are the residuals in Mróz et al. (2022) and the Lam et al. (2022a, 2022b) EW model. The residuals in Lam et al. (2022a, 2022b) are somewhat larger than expected in R.A. due to the model being a poor fit to the data. The residuals in Sahu et al. (2022) are smaller than expected, possibly indicative of underestimated uncertainties.

To be more quantitative, we also perform an Anderson–Darling (A-D) test to check whether the distribution of normalized residuals is consistent with a standard normal distribution. Table 7 lists the the A-D test S-statistic, for the model fits in R.A. and decl. The critical values for significance levels of 5% and 1% are 0.709 and 0.984, respectively. Thus,

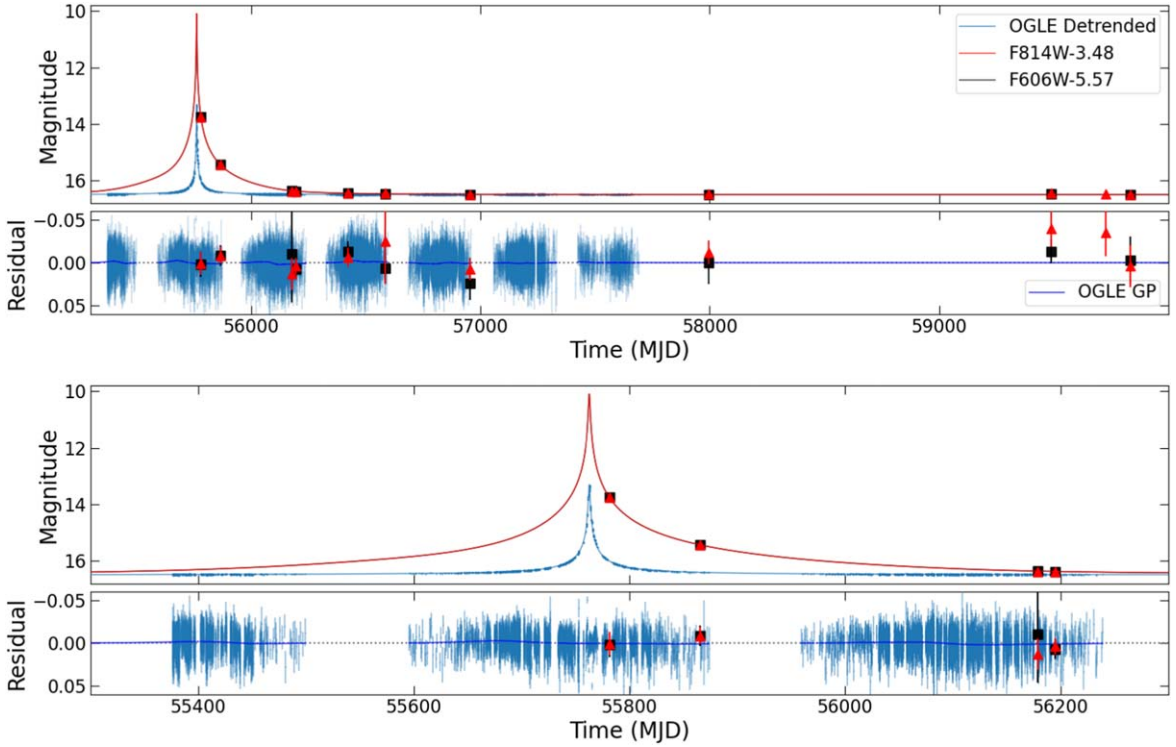

Figure 8. Top panel: HST F814W (red triangles), HST F606W (black squares), and detrended OGLE light curves (blue), with the corresponding maximum likelihood estimator (MLE; described in Section 5) plotted over the data. Second from top panel: residuals to the MLE model. The Gaussian process (GP) model is plotted on top of the OGLE residuals. Second from bottom panel: same as the top panel, but zoomed into the three most magnified years (2010–2012). Bottom panel: same as the second from top panel, but zoomed into the three most magnified years (2010–2012).

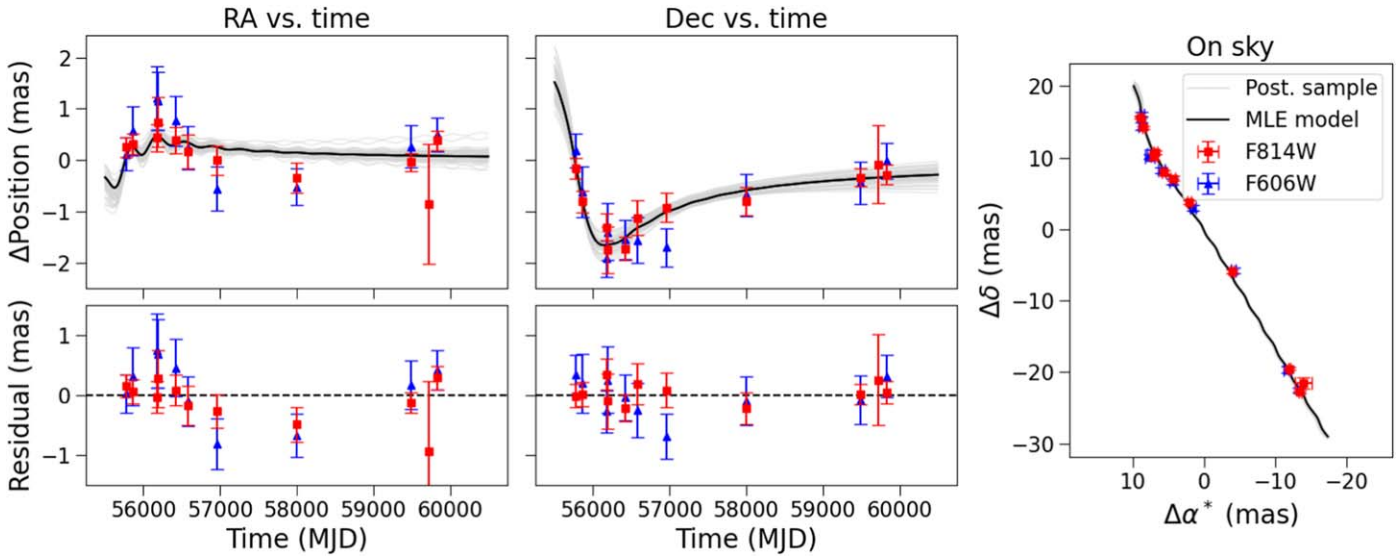

Figure 9. OB110462 astrometry. Left column, top to bottom: R.A. vs. time with MLE unlensed source motion model subtracted; residuals to the MLE model for R.A. vs. time fit. HST F814W astrometric data are shown in red; HST F606W astrometric data are shown in blue. The MLE model is shown in black. Fifty random draws from the posterior distribution are shown in light gray. Middle column, top to bottom: same as the left column, except for decl. instead of R.A. Right panel: astrometry as seen on sky, in the barycentric frame.

all models presented are consistent with being drawn from a standard normal distribution.

6.3. Bias-correction Method

We find the main difference in the astrometry between this work and Lam et al. (2022a, 2022b) stems from the bias correction. The other changes in the astrometric analysis did not significantly change the astrometry; we show this along with more detailed comparisons in Appendix C.

We compare the measured photometric and astrometric bias corrections due to the bright neighbor star in Figure 12. Using `hst1pass`, we find the average positional bias in the unmagnified epochs is around 1.6 mas in F814W and 0.6 mas in F606W (also see Figure 4 and Table 2). These are two to three times larger than the bias found by Lam et al. (2022b)

Table 3
HST Calibrated Data

Epoch	R.A. (mas)	Decl. (mas)	Mag (Vega)
F814W			
2022-09-13	-13.43 ± 0.19	-22.75 ± 0.19	19.965 ± 0.024
2022-05-29	-13.91 ± 1.17	-21.55 ± 0.76	19.926 ± 0.027
2021-10-01	-11.93 ± 0.17	-19.53 ± 0.17	19.921 ± 0.021
2017-08-29	-3.97 ± 0.29	-5.88 ± 0.27	19.949 ± 0.014
2014-10-26	2.11 ± 0.29	3.81 ± 0.28	19.964 ± 0.013
2013-10-22	4.32 ± 0.33	7.10 ± 0.34	19.918 ± 0.050
2013-05-13	5.62 ± 0.26	8.01 ± 0.23	19.916 ± 0.011
2012-09-25	7.04 ± 0.48	10.17 ± 0.46	19.849 ± 0.010
2012-09-09	6.83 ± 0.27	10.76 ± 0.26	19.846 ± 0.018
2011-10-31	8.47 ± 0.20	14.23 ± 0.21	18.897 ± 0.009
2011-08-08	8.87 ± 0.19	15.65 ± 0.20	17.230 ± 0.014
F606W			
2022-09-13	-13.31 ± 0.33	-22.48 ± 0.35	22.054 ± 0.028
2021-10-01	-11.63 ± 0.41	-19.63 ± 0.41	22.043 ± 0.014
2017-08-29	-4.15 ± 0.36	-5.76 ± 0.41	22.056 ± 0.025
2014-10-26	1.56 ± 0.42	3.03 ± 0.38	22.076 ± 0.019
2013-10-22	4.39 ± 0.42	6.66 ± 0.45	22.046 ± 0.018
2013-05-13	5.99 ± 0.48	8.18 ± 0.39	22.005 ± 0.012
2012-09-25	7.45 ± 0.57	10.52 ± 0.56	21.948 ± 0.011
2012-09-09	7.59 ± 0.62	10.15 ± 0.35	21.918 ± 0.057
2011-10-31	8.72 ± 0.48	14.41 ± 0.49	20.992 ± 0.012
2011-08-08	8.74 ± 0.32	16.00 ± 0.33	19.326 ± 0.015

Note. Relative positions and magnitudes of OB110462.

using `ks2` (see Figures 22 and 23 in Lam et al. 2022b; the "Neighbor-like" columns). This suggests that PSF fitting in `ks2` is more precise than in `hst1pass`.

Similar to Lam et al. (2022b), there is minimal positional and magnitude bias in the first epoch, where OB110462 and the neighbor are of roughly equal brightness. In the third epoch onwards, the bias becomes nonnegligible when OB110462 is much fainter, and the bias is primarily in the radial direction in F814W, and more mixed between radial and azimuthal in F606W. We find that the magnitude bias to be also larger in `hst1pass` than in `ks2`. The average bias in unmagnified epochs is around 15 mmag in F814, and about 5 mmag in F606W when using `ks2`, as compared to around 50 mmag in F814W and 20 mmag in F606W when using `hst1pass`. This again suggests that PSF fitting in `ks2` is more precise than in `hst1pass`.

The `hst1pass` positional bias, when averaged across the two filters, is comparable to the bias of 1.2 mas[1] found by Sahu et al. (2022). This is true, even though different sets of stars were used to compute the bias (18 versus 4) as well as different methods (PSF subtraction versus artificial star-planting tests).

The results imply that combining relative measurements across `ks2` and `hst1pass` is not valid. Although the majority of the underlying source extraction algorithms are identical, the particulars of PSF fitting are different enough to alter the measured positions significantly. The two software source extraction methods cannot be combined together in a self-consistent manner. Thus, the positional bias as calculated in Lam et al. (2022a, 2022b) was too small, and resulted in an incorrect set of astrometric measurements.

[1] Sahu et al. (2022) do not specify the bias as a function of filter; we assume that their stated bias of 1.2 mas is the average of F606W and F814W.

Table 4
Posterior Distributions of the Fit Parameters

Parameter	$\mathrm{Med}^{+1\sigma}_{-1\sigma}$	MAP	MLE
t_0 (MJD)	$55764.47^{+0.85}_{-0.93}$	55764.69	55763.84
u_0	$-0.05^{+0.007}_{-0.007}$	−0.05	−0.05
t_E (days)	$275.98^{+5.23}_{-6.01}$	267.26	287.48
$\log_{10}(\theta_\mathrm{E}/\mathrm{mas})$	$0.68^{+0.05}_{-0.06}$	0.68	0.69
π_S (mas)	$0.11^{+0.02}_{-0.02}$	0.09	0.12
$\pi_{\mathrm{E,E}}$	$0.03^{+0.005}_{-0.005}$	0.03	0.02
$\pi_{\mathrm{E,N}}$	$-0.09^{+0.01}_{-0.01}$	−0.10	−0.09
$x_{\mathrm{S0,E}}$ (mas)	$230.31^{+0.11}_{-0.11}$	230.32	230.35
$x_{\mathrm{S0,N}}$ (mas)	$-214.76^{+0.16}_{-0.16}$	−214.90	−214.73
$\mu_{\mathrm{S,E}}$ (mas yr^{-1})	$-2.02^{+0.01}_{-0.01}$	−2.02	−2.02
$\mu_{\mathrm{S,N}}$ (mas yr^{-1})	$-3.45^{+0.02}_{-0.02}$	−3.45	−3.45
$b_{\mathrm{SFF,O}}$	$0.05^{+0.002}_{-0.001}$	0.05	0.05
$m_{\mathrm{base,O}}$ (mag)	$16.48^{+0.0004}_{-0.0004}$	16.49	16.49
$b_{\mathrm{SFF},H8}$	$0.98^{+0.03}_{-0.03}$	0.93	0.98
$m_{\mathrm{base,H8}}$ (mag)	$19.96^{+0.005}_{-0.005}$	19.96	19.96
$b_{\mathrm{SFF},H6}$	$0.98^{+0.03}_{-0.03}$	0.95	0.98
$m_{\mathrm{base,H6}}$ (mag)	$22.05^{+0.006}_{-0.006}$	22.05	22.06
M_L ($M_\odot$)	$6.03^{+1.19}_{-1.04}$	5.40	6.39
π_L (mas)	$0.58^{+0.09}_{-0.09}$	0.60	0.58
π_rel (mas)	$0.47^{+0.09}_{-0.09}$	0.52	0.45
$\mu_{L,E}$ (mas yr^{-1})	$-3.80^{+0.48}_{-0.55}$	−3.84	−3.50
$\mu_{L,N}$ (mas yr^{-1})	$2.60^{+0.83}_{-0.80}$	2.80	2.53
$\mu_{\mathrm{rel,E}}$ (mas yr^{-1})	$1.78^{+0.56}_{-0.48}$	1.82	1.49
$\mu_{\mathrm{rel,N}}$ (mas yr^{-1})	$-6.05^{+0.82}_{-0.83}$	−6.25	−5.98
θ_E (mas)	$4.79^{+1.13}_{-1.15}$	4.76	4.85
π_E	$0.10^{+0.01}_{-0.01}$	0.05	0.10
$\delta_{\mathrm{c,max}}$ (mas)	$1.69^{+0.40}_{-0.41}$	1.68	1.72

Note. The columns list the median (med) $\pm 1\sigma$ (68%) credible intervals, maximum a posteriori (MAP) solution, and MLE solution for the microlensing model parameters.

Table 5
Summary of the Data and Models in the Different Analyses

Reference	OGLE data	HST data	Likelihood
This work	Updated	2011–2022	DW
Lam et al. (2022a, 2022b); DW	Original	2011–2021	DW
Lam et al. (2022a, 2022b); EW	Original	2011–2021	EW
Sahu et al. (2022)	Original	2011–2017	DW
Mroz et al. (2022)	Updated	2011–2017	DW

Note. OGLE data: "Original" is the original OGLE reduction of OB110462 used in Lam et al. (2022a, 2022b) and Sahu et al. (2022); "Updated" is the OGLE rereduction of OB110462 presented in Mróz et al. (2022). HST data: the time span listed indicates the years of HST data used. Likelihood: "DW" is the likelihood used in performing the model fit that weights each data point equally; "EW" is the likelihood that weights the OGLE photometry, HST photometry, and HST astrometry equally.

In addition, Section 4.2.5 of Lam et al. (2022b) noted an "astrometric color offset" between the F814W and F606W positions of OB110462 and another microlensing event called OB110037. For OB110462, the astrometry across the F814W and F606W filters was offset from each other by about 0.5 mas. This color difference was tentatively attributed to binarity. For OB110462, this color difference can mainly be attributed to the

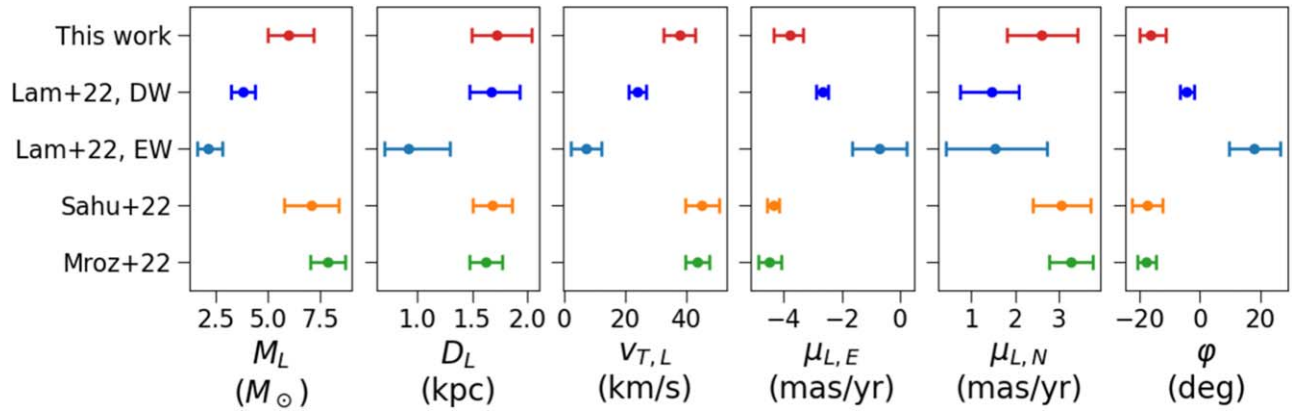

Figure 10. Comparison of the lens mass M_L, distance D_L, transverse velocity $v_{T,L}$, proper motion vector ($\mu_{L,E}$, $\mu_{L,N}$), and lens–source relative proper motion direction φ inferred from the various studies of OB110462.

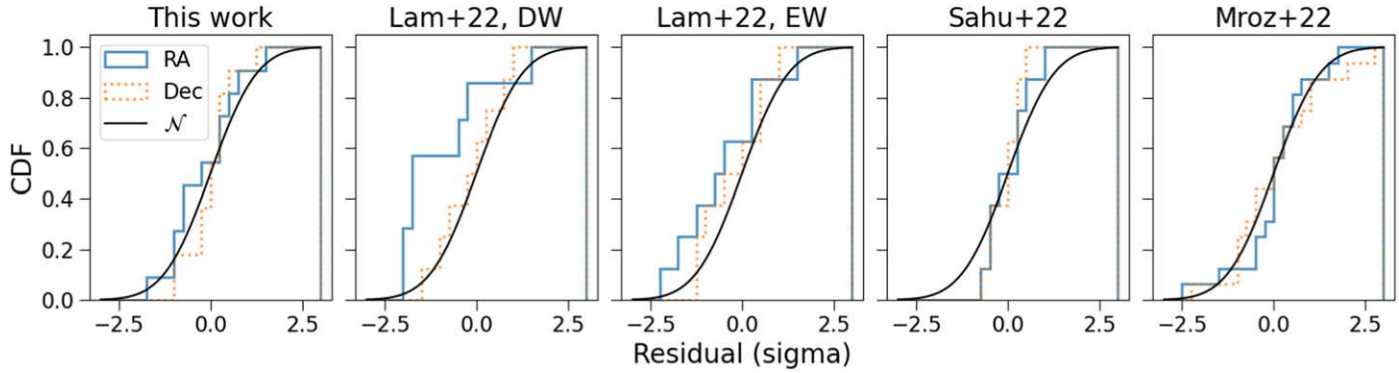

Figure 11. CDF of normalized residuals for astrometric models and data, as compared to the CDF of a standard normal distribution. The CDF of normalized residuals for the astrometry in R.A. (decl.) is shown in the blue solid (orange dotted) line. The CDF of a standard normal distribution is shown as the black curve.

Table 6
Comparison of the Lens Properties

Reference	M_L ($M_\odot$)	D_L (kpc)	$v_{T,L}$ (km s^{-1})	$\mu_{L,E}$ (mas yr^{-1})	$\mu_{L,N}$ (mas yr^{-1})	φ (deg)
This work	$\mathbf{6.03}^{+1.19}_{-1.04}$	$\mathbf{1.72}^{+0.32}_{-0.23}$	$\mathbf{37.61}^{+5.12}_{-5.13}$	$\mathbf{-3.80}^{+0.48}_{-0.55}$	$\mathbf{2.60}^{+0.83}_{-0.80}$	$\mathbf{343.75}^{+4.80}_{-3.95}$
Lam et al. (2022a, 2022b); DW	$3.79^{+0.62}_{-0.57}$	$1.67^{+0.26}_{-0.20}$	$23.95^{+2.95}_{-2.95}$	$-2.64^{+0.18}_{-0.24}$	$1.46^{+0.63}_{-0.71}$	$355.47^{+2.66}_{-2.11}$
Lam et al. (2022a, 2022b); EW	$2.15^{+0.67}_{-0.54}$	$0.92^{+0.38}_{-0.22}$	$7.26^{+4.88}_{-4.88}$	$-0.69^{+0.91}_{-0.94}$	$1.53^{+1.21}_{-1.12}$	$18.08^{+8.60}_{-8.31}$
Sahu et al. (2022)	7.1 ± 1.3	1.58 ± 0.18	$\sim 45 \pm 5.5$	-4.36 ± 0.22	3.06 ± 0.66	342.5 ± 4.9
Mroz et al. (2022)	7.88 ± 0.82	1.62 ± 0.15	43.4 ± 3.8	-4.48 ± 0.39	3.29 ± 0.5	342.3 ± 3.0

Note. Comparison of the lens mass M_L, distance D_L, transverse velocity $v_{T,L}$, proper motion vector ($\mu_{L,E}$, $\mu_{L,N}$), and lens–source relative proper motion direction φ inferred from the various studies of OB110462.

bias correction (Figure 13). However, the color differences between OB110037 and the other stars are still unexplained.

7. Discussion

7.1. OB110462 in the Context of the Galactic BH Population

Before 2019, all information about Galactic BHs came from X-ray binary systems, mainly low-mass X-ray binaries (LMXBs). The observed population of BHs in LMXBs have masses tightly centered around $\sim 8\ M_\odot$ (Özel et al. 2010).

A portrait of the complete Galactic BH population is finally emerging (Figure 14; X-ray sources were compiled across catalogs from Aaron Geller (Northwestern),[2] Grzegorz Wiktorowicz and Chris Belczynski,[3] and BlackCAT[4] (Corral-Santana et al. 2016)). Over the last 5 yr, our knowledge of other types of Galactic BH systems has grown. The first BH in a

Table 7
A-D Test Statistic

Work	R.A.	Decl.
This work	0.39	0.24
Lam et al. (2022a, 2022b); DW	0.64	0.24
Lam et al. (2022a, 2022b); EW	0.17	0.27
Sahu et al. (2022)	0.22	0.40
Mroz et al. (2022)	0.50	0.29

[2] https://github.com/ageller/LIGO-Virgo-Mass-Plot_v2.0/blob/main/src/data/EMdata.json

[3] https://stellarcollapse.org/sites/default/files/table.pdf

[4] https://www.astro.puc.cl/BlackCAT/transients.php

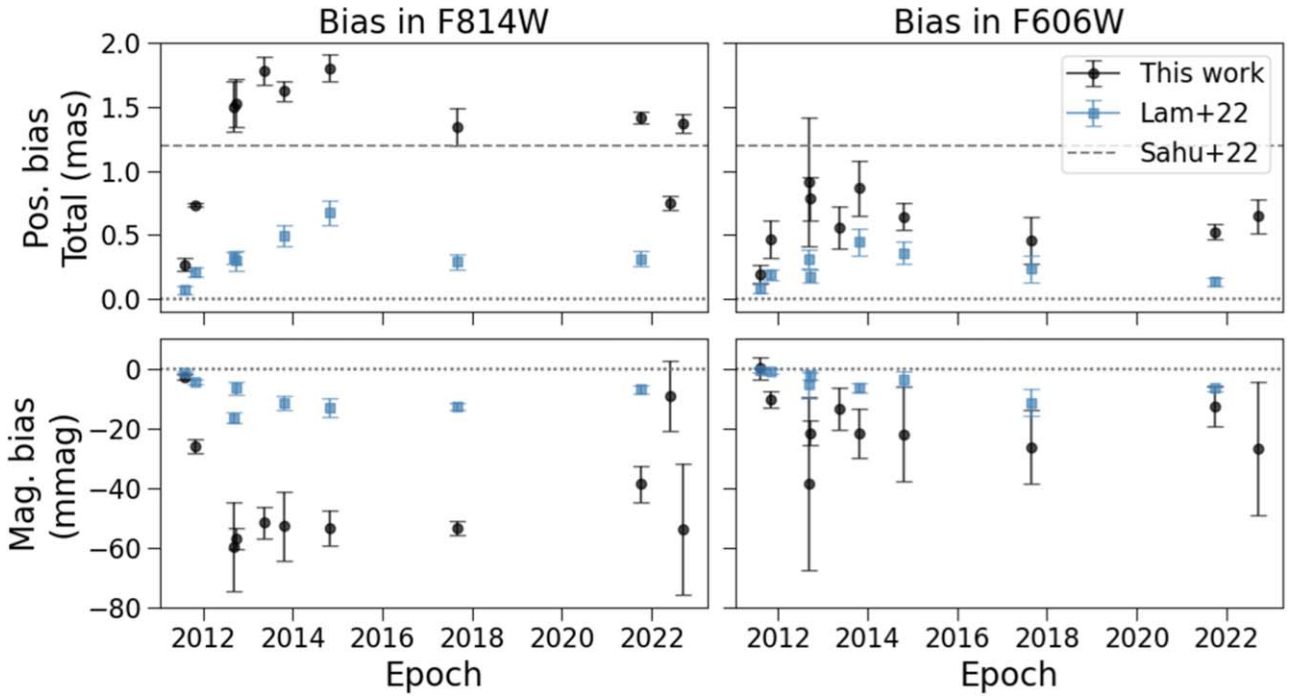

Figure 12. Comparison of the bias correction measured in this work to those in Lam et al. (2022b) and Sahu et al. (2022). The left (right) column shows the bias in F814W (F606W). The top (bottom) row shows the astrometric (photometric) bias, where the bias is defined as the recovered minus injected value. The biases measured in this work performed using injection-and-recovery tests with `hst1pass` are shown in black circles. The biases measured in Lam et al. (2022b) performed using injection-and-recovery tests with `ks2` are shown as light blue squares. The astrometric bias reported by Sahu et al. (2022) performing PSF subtraction is shown as the dashed gray line. Sahu et al. (2022) report a single value for the astrometric bias; we show this same value in both the F814W and F606W panels.

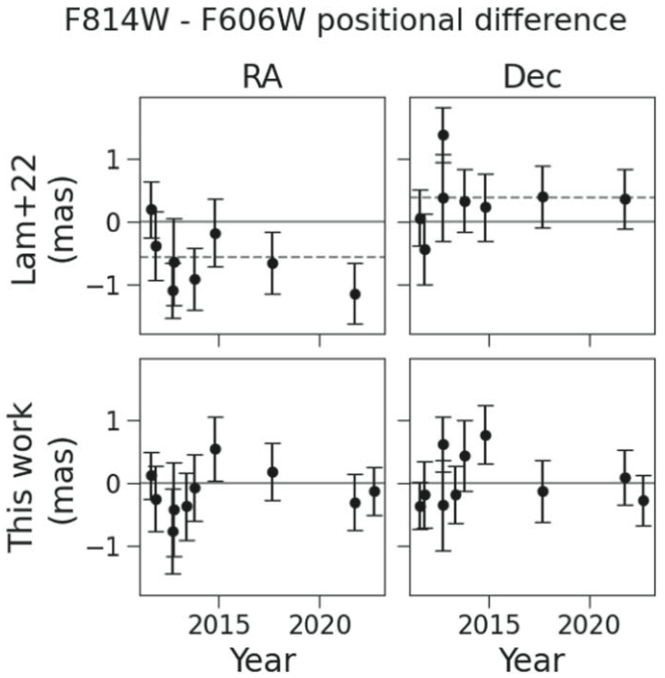

Figure 13. Comparison of the color differences in OB110462 astrometry. The top row shows the difference in F606W and F814W position for OB110462 vs. time from Lam et al. (2022a, 2022b). The bias correction calculated in Lam et al. (2022b) has been applied, but the constant positional offset between F814W and F606W is not included. The dashed line is the "empirical color offset" applied by Lam et al. (2022b) to get the data in the two filters to agree better with each other. There is a significant difference between the positions measured between the two filters, especially in R.A. The bottom row shows the difference in the F606W and F814W positions for OB110462 vs. time as derived in this work. The color difference has largely disappeared from the R. A. and also slightly decreased in decl.

noninteracting system was found to have a somewhat surprising low mass of 3 $M_\odot$, in the "lower mass gap" where neutron stars and BHs had not previously been observed electromagnetically (Thompson et al. 2019). Since then, two more BHs in noninteracting binary systems have been found, with masses of 9–10 $M_\odot$ (Chakrabarti et al. 2023; El-Badry et al. 2023a, 2023b). This is somewhat higher than the average observed BH mass in an LMXB, but falls within the typical mass range.

Now, OB110462 is the first isolated BH to have its mass measured. At 6 $M_\odot$, it is slightly less massive than the average observed BH mass in an LMXB, although still falling within the typical mass range.

The selection effects that affect observations of BHs are important to consider if we are to understand the underlying population and BH mass function. For example, observational selection effects may cause more massive BHs in LMXBs to be undetected (Jonker et al. 2021). For BHs in detached binaries, the picture is more muddled: there is tentative evidence of a dearth of BHs below 8 $M_\odot$ (El-Badry et al. 2023b) as detected from Gaia, but ground-based radial velocity surveys seem to not be finding these more massive BHs and have only found a single low-mass BH despite an observational bias toward higher masses (Thompson et al. 2019). For isolated BHs, there is also a selection bias toward more massive BHs as they have larger lensing cross sections; however, if there are many more low-mass BHs, those will dominate the observed sample. With one detection, no strong conclusions can be made, but there should be at least as many 6–8 $M_\odot$ BHs as 10 $M_\odot$ BHs in the Galactic BH population.

Figure 15 compares OB110462 to a simulated population of Galactic microlensing events. OB110462 is somewhat unusual compared to typical microlensed BHs—it has a relatively large

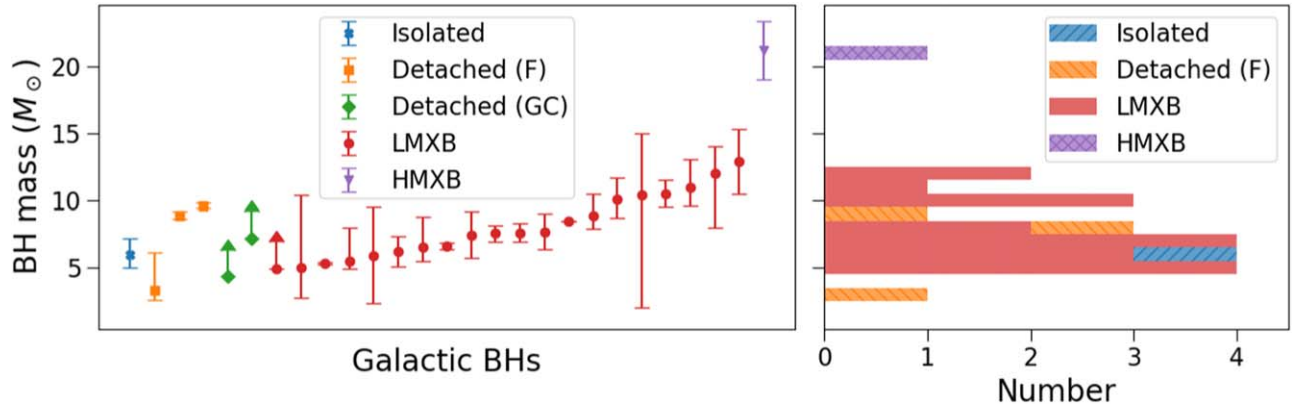

Figure 14. OB110462 in the context of the observed Galactic BH population. Left: dynamically confirmed BHs, coded by their type (isolated, detached field binary, detached globular cluster binary, LMXB, and high-mass X-ray binary). Right: histogram of Galactic BH mass measurements, coded by type. Note that not all BHs in the left panel are included in the right panel, as some only have lower limits on the mass. Note the histogram does not account for the uncertainties on the measurements.

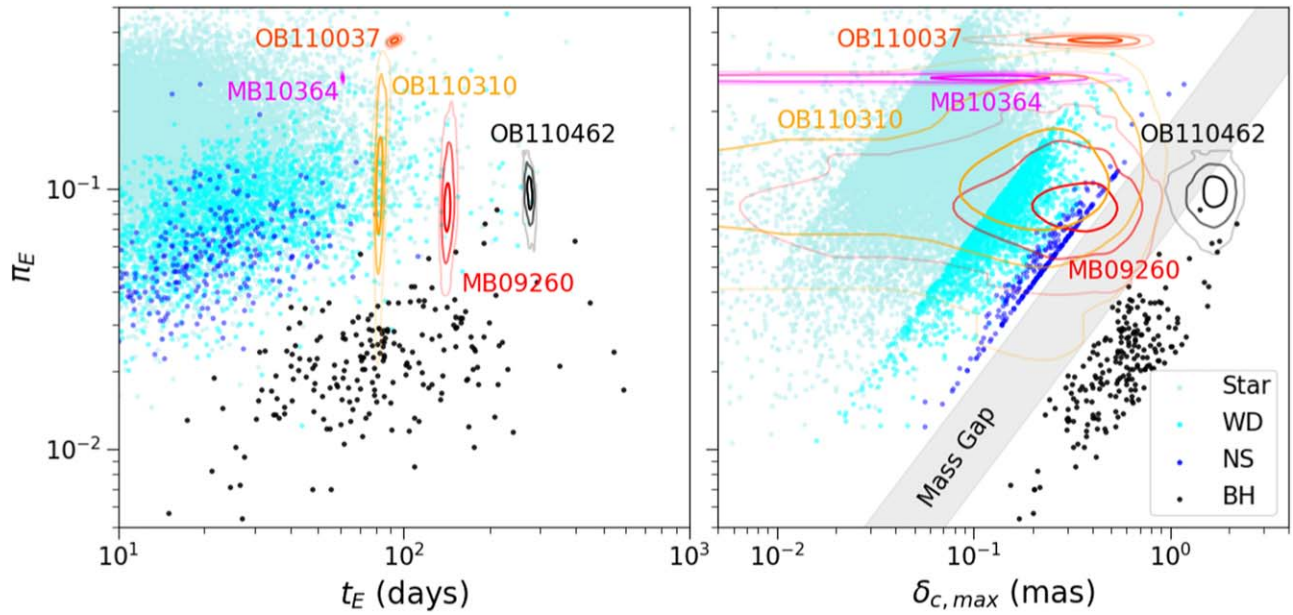

Figure 15. Microlensing parallax π_E vs. Einstein crossing time t_E (left) and maximum astrometric shift $\delta_{c,max}$ (right) of five BH microlensing candidates analyzed in Lam et al. (2022a, 2022b). It is the same as Figure 6 of Lam et al. (2022a), except the contours for OB110462 have been updated with the values inferred in this work. MB09260, MB10364, OB110037, and OB110310 are low-mass ($<4\ M_\odot$) lenses and not BHs. The points are simulated microlensing events from the `PopSyCLE` microlensing simulation (Lam et al. 2020). Compared to the simulated BH population, OB110462 has a relatively large astrometric shift, large microlensing parallax, and long Einstein crossing time.

astrometric shift for its mass, as well as a large microlensing parallax for a BH. This is due to OB110462 being a nearby (<2 kpc) lens; its large astrometric shift and microlensing parallax facilitated its detection and characterization.

Now that detections of BHs in various types of systems have been made, understanding their selection effects are needed to quantify their population properties. This is the next research frontier that will enable us to understand the Galactic BH population as a whole.

7.2. Origin and Formation Scenarios for OB110462

With only a single isolated BH detection, tight constraints cannot be placed yet on their origins or specific formation scenarios. In addition, OB110462 does not have full 6D kinematic information available, since microlensing does not measure the lens' radial velocity. However, recent works examine possible situations that are consistent with observations of OB110462 and lay the groundwork for future studies.

Using statistical arguments and assuming OB110462 originated from a single star, Andrews & Kalogera (2022) finds that OB110462 is kinematically consistent with the Galactic thick disk. Given the mass, distance, and transverse velocity found in this work, if OB110462 was born in the thick disk, natal kicks up to 100 km s^{-1} would be consistent with its current velocity. On the other hand, if OB110462 formed in the thin disk and received a kick to a thick disk-like orbit, the kick would have had to be around 50–100 km s^{-1}.

Vigna-Gómez & Ramirez-Ruiz (2023) study the origins of isolated BHs. They find that the majority of BHs with masses $<10\ M_\odot$ originated from binary systems, while the majority of BHs with masses $>10\ M_\odot$ originated as single stars. This would imply that although OB110462 is now an isolated BH, it likely originated in a stellar binary system.

With additional mass measurements of isolated BHs, these studies and their extensions will be able to place increasingly tighter constraints on the formation channels and origins of isolated BHs. By performing targeted astrometric follow up with existing facilities, it is possible to build the sample of isolated BHs to a few ($\lesssim$10) over the next 5–10 yr.

7.3. Toward a Large Sample of Isolated BHs

Lam et al. (2022a, 2022b) analyzed a sample of five archival BH microlensing candidates, which included OB110462. The other four candidates were not BHs. They found that after accounting for selection effects, this single BH detection was consistent with 2×10^8 isolated Galactic BHs. Although the results were consistent, they were not highly constraining due to the small sample size. The Nancy Grace Roman Space Telescope (Roman), NASA's next flagship mission, presents an opportunity to find and characterize hundreds of isolated BHs with astrometric microlensing (Lam et al. 2020), which will expand the sample size and enable stringent constraints on the Galactic BH population.

Roman will conduct several wide-field infrared surveys to answer questions about dark energy and dark matter, and find exoplanets (Spergel et al. 2015). One of the surveys, the Galactic Bulge Time Domain Survey, nominally plans to observe $\sim$2 degree^2 of the Galactic Bulge, finding several tens of thousands of microlensing events and a thousand exoplanets (Penny et al. 2019; Johnson et al. 2020). This survey also provides an excellent opportunity to find isolated BHs with microlensing.

OB110462, in addition to being a proof of concept of the method, raises several technical issues that have not been previously considered, and should be examined in preparation for using microlensing to find BHs with Roman.

Roman's mirror is the same size as Hubble (a diameter of 2.4 m), but will be observing at longer wavelengths than the optical bands used for this and most other microlensing work. Thus the bias due to a nearby star in an event like OB110462 would be larger.

Roman will also be similarly or more undersampled than HST. Roman's pixel scale is 110 mas pixel^{-1}; the main filter for the Galactic Bulge Time Domain Survey is nominally F146, a wide filter centered at 1.46 μm, corresponding to an angular resolution of $\theta_{\rm res} = 153$ mas at the diffraction limit. For comparison, the HST WFC3/UVIS pixel scale is 40 mas pixel^{-1}; the resolution at the effective wavelength of F814W = 814 nm (F606W = 606 nm) is 85 (64) mas. Thus, these PSF reconstruction and modeling methods currently required to achieve precise astrometry with HST will also be necessary for Roman.

In addition, the density of sources will be much higher in the infrared than in the (red) optical. Roman will observe hundreds of millions of stars down to twenty-fifth magnitude in F146, exacerbating this issue. In addition, if Roman chooses to observe fields closer to the Galactic Plane toward $b = 0°$, the density of sources will also increase. Finally, Roman's field of view will be 200 times that of Hubble's in the infrared. Events like OB110462, where a faint source of interest is near a bright one, will be common and not necessarily an ignorable edge case. A more automated or generalized way to correct the photometry and astrometry in this situation will be needed.

This also will have impact on the assumptions made in astrometric measurements. This work as well as previous studies (Lu et al. 2016; Lam et al. 2022a, 2022b; Sahu et al. 2022) assume that the astrometric shift measured is completely unblended; i.e., the lens is dark, there are no unrelated neighboring stars, and the only light that makes it to the telescope aperture is from the images of the source. However, for all the reasons mentioned above, this assumption will not necessarily hold for Roman. Despite the resolution gain from going to space, there is expected to be a nonnegligible fraction of blended microlensing events (Penny et al. 2019). For dark lenses like BHs, the concern of blending would be from unrelated neighbor stars falling in Roman's aperture. This extra flux would dilute the astrometric signal. In addition, if the proper motion of the neighbor(s) was comparable to the lensing, it could affect not only the magnitude, but the shape of the astrometric shift.

Other considerations are how to perform relative astrometry best over such large fields of view. The details of detector-to-detector calibration issues will be important. Design trade-offs in terms of observing strategy in order to attain sufficient astrometric precision should also be studied. All the statements made here are qualitative, but these issues deserves further quantitative study.

8. Conclusion

We reanalyze OB110462, a microlensing event due to a dark, compact-object lens. The astrometry we measure is significantly different from Lam et al. (2022a, 2022b); the discrepancy is caused by a difference in the measured bias correction from a neighboring bright star. By performing both the astrometric source extraction and bias-correction measurement with the new version of `hst1pass` in a self-consistent manner, we find our astrometry for OB110462 between 2011 and 2017 to be consistent with Sahu et al. (2022). Modeling the updated HST photometry and astrometry along with the rereduced OGLE photometry, we find OB110462 to be a BH with a mass of $6.03^{+1.19}_{-1.04} M_\odot$, consistent with the measurement of Sahu et al. (2022). Thus, it appears so far that the masses of isolated Galactic BHs are similar to those in binary systems. With the Roman Space Telescope, many more isolated BH systems can be characterized, and ultimately enable the measurement of the Galactic BH mass function.

Acknowledgments

C.Y.L. and J.R.L. acknowledge support from the National Science Foundation under grant No. 1909641 and the Heising-Simons Foundation under grant No. 2022-3542. C.Y.L. also acknowledges support from NASA FINESST grant No. 80NSSC21K2043 and a research grant from the H2H8 Foundation.

We thank the anonymous referee and Dan Weisz for helpful comments that improved the manuscript. We thank Kailash Sahu, Howard Bond, and Jay Anderson for proposing and taking the HST SNAP observation used in this work. We additionally thank Jay Anderson for developing `hst1pass` and his helpfulness and responsiveness to questions and comments on the software.

This research has made use of NASA's Astrophysics Data System. Some of the data presented in this paper were obtained from the Mikulski Archive for Space Telescopes (MAST) at the Space Telescope Science Institute. The specific observations analyzed can be accessed via doi:10.17909/gpw0-w659.

Appendix A
Comparison of Pixel-based versus Tabular CTE Corrections

Here we compare the differences between the tabular and pixel-based CTE corrections. The differences alone do not indicate which type of correction is better or worse, but allows us to quantify the differences in the resultant astrometry.

Specifically, the comparison is made between the starlists in Lam et al. (2022a, 2022b) created using the pixel-based CTE correction (i.e., the old version of `hst1pass` run on the `flc` files) as compared to the starlists in this work created using the tabular CTE correction (i.e., the new version of `hst1pass`, run on the `flt` files). Several frames spanning 10 yr of the OB110462 data set are shown in Figure 16.

As a function of the detector's y-position, there are only differences between the y-position and instrumental magnitude; the differences are symmetric in the detector's x-position. This is expected, since CTE corrections only change the detector's y-position and magnitude of the sources. The scatter in x-position is likely due to minor differences between the versions of `hst1pass` and differences in the choices of certain runtime parameters between the old and new reductions. The scatter in the x-position also allows us to see how much of the trend in the y-position is due to scatter, versus the CTE-correction methods themselves. As time goes on, the scatter increases greatly in the x- and y-position differences. The scatter also seems to increase with time for magnitude difference, although it is mostly constant after 2013 or so.

As a function of magnitude, the differences are again symmetric about the x-position, but not for the y-position and magnitude. In particular, for the differences in y-position before 2013, bright stars with $m < -10$ are not affected, but after 2013 there is magnitude-dependent structure.

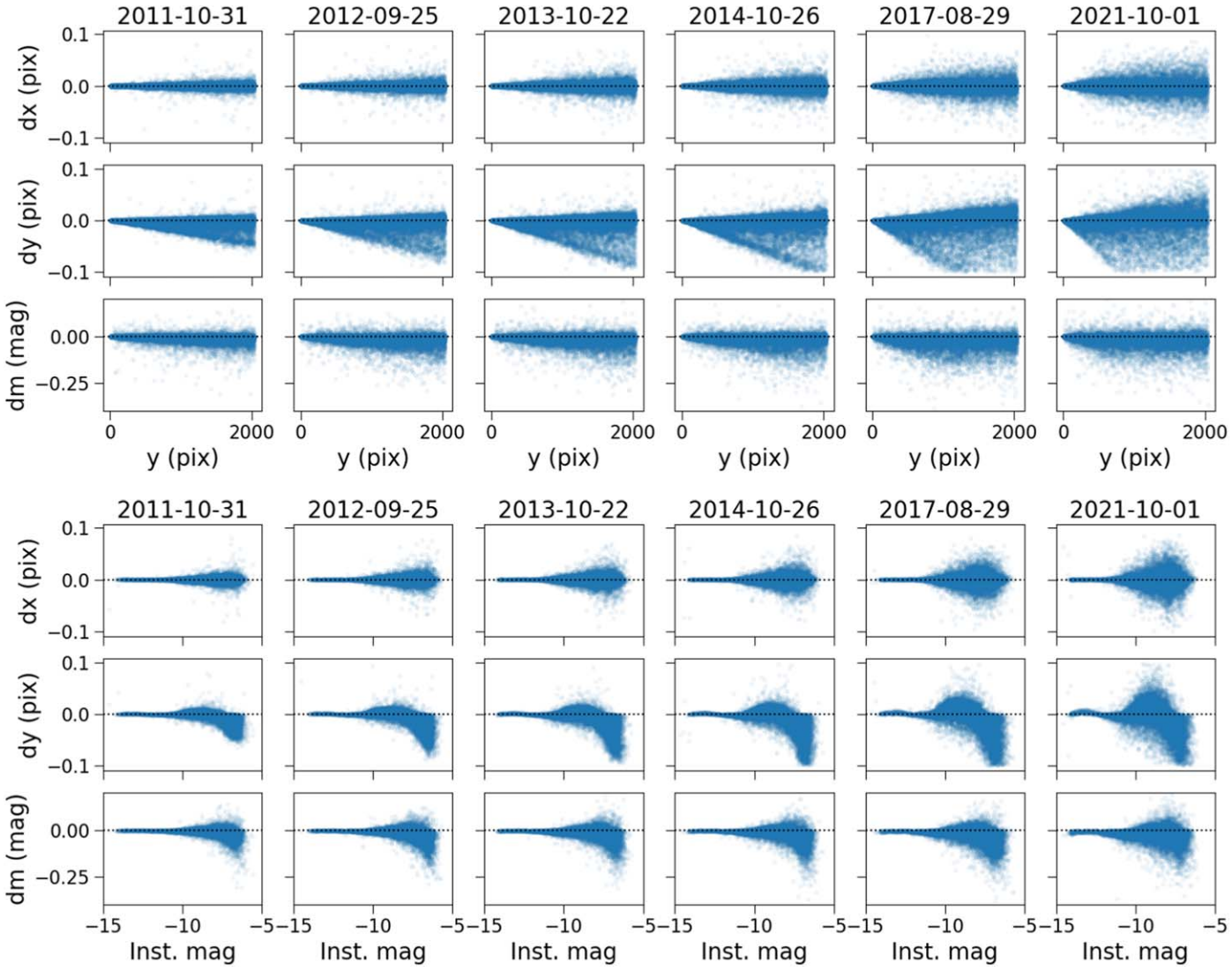

Figure 16. Comparison of the measured positions and magnitudes using the new `hst1pass` and tabular CTE correction vs. the old `hst1pass` and pixel-based CTE correction. These comparisons are performed on a single exposure, i.e., on the individual `flc.xym` or `flt.XYM` files. The y-axis is the difference between the new tabular and old pixel-based correction for the detector's x-position, y-position, and instrumental magnitude. The top (bottom) plot shows the differences as a function of the detector's y-position (instrumental magnitude).

Appendix B
Priors

The priors for the fits are summarized in Table 8. $\mathcal{N}(\mu, \sigma)$ denotes a normal distribution with mean μ and standard deviation σ. $\mathcal{N}_T(\mu, \sigma, l_\sigma, u_\sigma)$ denotes a normal distribution with a low-end truncation at $\mu + \sigma l_\sigma$ and a high-end truncation at $\mu + \sigma u_\sigma$. $\mathcal{U}(a, b)$ denotes a uniform distribution from a to b. $\Gamma^{-1}(\alpha, \beta)$ is the inverse gamma distribution (Equation G1 in Lam et al. 2022b).

The choices of priors are nearly identical to those in Lam et al. (2022a, 2022b); see Appendix G of Lam et al. (2022b) for details. The only difference is for the photometric priors $b_{\rm SFF}$ and $m_{\rm base}$. We changed the priors on $m_{\rm base}$ as some of the photometry was recalibrated and the baseline magnitudes were now different. We also made the priors on $b_{\rm SFF}$ tighter; the blending is well constrained from previous work (Lam et al. 2022a; Mróz et al. 2022; Sahu et al. 2022). We did allow for some spread, but consider it well established that the OGLE light curve is highly blended ($b_{\rm SFF}$ close to 0) and the HST light curves are less or unaffected by blending ($b_{\rm SFF}$ close to 1).

Table 8
Priors

Parameter	Prior
t_0 (MJD)	$\mathcal{N}(55770, 75)$
u_0	$\mathcal{N}(0, 0.5)$
$t_{\rm E}$ (days)	$\mathcal{N}_T(200, 100, -1.8, 3)$
$\pi_{\rm E,E}$	$\mathcal{N}(-0.02, 0.12)$
$\pi_{\rm E,N}$	$\mathcal{N}(-0.03, 0.13)$
$m_{\rm base,O}$ (mag)	$\mathcal{N}(16.5, 0.1)$
$b_{\rm SFF,O}$	$\mathcal{U}(0, 0.2)$
$m_{\rm base,H8}$ (mag)	$\mathcal{N}(19.9, 0.1)$
$b_{\rm SFF,H8}$	$\mathcal{U}(0.8, 1.1)$
$m_{\rm base,H6}$ (mag)	$\mathcal{N}(22.0, 0.1)$
$b_{\rm SFF,H6}$	$\mathcal{U}(0.8, 1.05)$
$\log \sigma_O$ (mag)	$\mathcal{N}(0, 5)$
ρ_O (days)	$\Gamma^{-1}(0.53, 0.31)$
$\log \omega_{0,O}^4 S_{0,O}$ (mag^2 days^{-3})	$\mathcal{N}(0.0001, 5)$
$\log \omega_{0,\rm O}$ (days^{-1})	$\mathcal{N}(0, 5)$
$\theta_{\rm E}$ (mas)	$\mathcal{N}_T(-0.2, 0.3, -4, 4)$
π_S (mas)	$\mathcal{N}_T(0.1126, 0.0213, -2.94, 90)$
$x_{S0,E}$ (arcsecond)	$\mathcal{U}(0.229, 0.233)$
$x_{S0,N}$ (arcsecond)	$\mathcal{U}(-0.240, -0.178)$
$\mu_{S,E}$ (mas yr^{-1})	$\mathcal{U}(-2.472, 2.515)$
$\mu_{S,N}$ (mas yr^{-1})	$\mathcal{U}(-2.354, 4.734)$

Appendix C
Detailed Comparison to Previous Work

C.1. CTE-correction Method

First, we compare the prebias-corrected astrometry presented in this work to that of Lam et al. (2022a, 2022b). The differences are the number of epochs of data used, the version of the `hst1pass` software, the values of the additive error, and the method of CTE correction. Of these differences, the method of CTE correction has the largest impact on the resultant astrometry.

We find no significant difference between the two astrometric time series after cross-epoch alignment and before implementing the bias correction. While the different CTE corrections can change the measured positions of stars by several milliarcseconds within a single epoch (Figure 16), these differences are effectively removed by the cross-epoch alignment when the starlists are transformed into a common reference frame using first- and second-order polynomials.

Thus, the specific choice of CTE-correction method, tabular or pixel-based, does not produce any significant change in the astrometric time series derived. It is only important that the CTE be corrected in some manner; in our previous work we find that if no CTE correction of any kind is applied, there are systematics in the astrometry that cannot be removed by the first- or second-order polynomial transformations.

C.2. Bias-corrected Astrometric Time Series

Figure 17 directly compares the astrometry of OB110462 in Sahu et al. (2022; their Figures 16 and 18), Lam et al. (2022a; their Figure 2), and this work. We emphasize that no microlensing model is being fit in Figure 17. Only a constant proper motion of (R.A., decl.) = (−2.263, −3.597) mas yr^{-1} has been subtracted from the positions for easier visualization. The subtracted proper motion was chosen to match the source proper motion inferred in Sahu et al. (2022) for an "apples-to-apples" comparison of the astrometry.

There is a clear discrepancy in the deflection in R.A. between the astrometry of Sahu et al. (2022) and Lam et al. (2022a, 2022b; top left panel) across the magnified epochs (2011) versus the unmagnified epochs (after 2011). There is some minor discrepancy in decl. (top right panel), but the measurements are generally within 1–2σ of each other. The new astrometry, including the updated bias correction, presented in this work is now consistent with the measurements of Sahu et al. (2022) between 2011 and 2017. In both R.A. (bottom left panel) and decl. (bottom right panel), the magnified and unmagnified astrometry are now all within 1σ of each other.

The new 2021–2022 measurements provide a more accurate source proper motion in baseline than in the previous work. From Figure 17, the source proper motion from our updated astrometric reductions appears to be different from that of Sahu et al. (2022). For $t \gg t_0$, the slope of the proper-motion-removed measurements should asymptotically approach 0. This is not the trend seen in the new 2021–2022 epochs, implying the source proper motion is different from the value inferred by Sahu et al. (2022). Although the source proper motion is not particularly interesting in and of itself, its inferred value affects the measured astrometric shift, which in turn affects the measured lens mass.

We consider whether these different proper motions could be the result of systematics in the analysis of the later epochs. No systematic errors of 1–2 mas in the 2021–2022 astrometry were detected in the reference stars (Figures 6 and 7).

The source proper motions inferred from the fit are presented in Table 4. The uncertainties in the transformation from the relative astrometric reference frame to the absolute Gaia reference frame in which the proper motions are reported are 0.13 mas yr^{-1} and 0.11 mas yr^{-1} in R.A. and decl., respectively. Sahu et al. (2022) do not state their uncertainties moving from their relative to absolute Gaia astrometric frame, but assuming their systematic uncertainties are comparable to

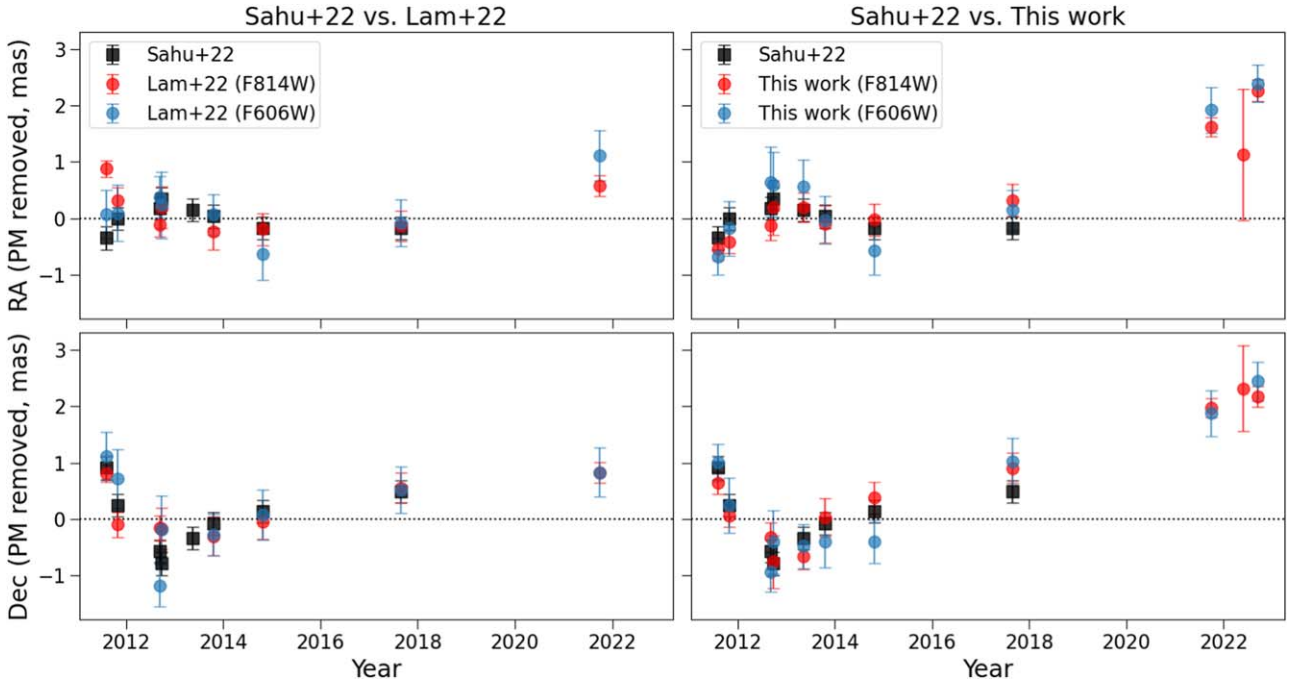

Figure 17. Comparison of the HST astrometry derived by Lam et al. (2022a, 2022b), Sahu et al. (2022), and this work. The top (bottom) row shows the astrometry in R.A. (decl.) vs. time, with the source proper motion reported in Sahu et al. (2022) (R.A. decl.) = (−2.263, −3.597) mas yr^{-1} subtracted in order to compare the astrometric deflections more easily. The left (right) column compares the astrometry in Sahu et al. (2022) to Lam et al. (2022a, 2022b) (this work). The positions of Sahu et al. (2022; black squares) are the average of all F814W and F606W measurements. Lam et al. (2022a, 2022b) and this work keep the F814W and F606W sets separate; the F814W (F606W) positions are shown in red (blue) circles.

ours, the source proper motion inferred in this work of (−2.02, −3.45) mas yr^{-1} and Sahu et al. (2022) of (−2.263, −3.597) mas yr^{-1} are consistent within 1–2σ. Thus, the source proper motions across the model fits are consistent with each other. However, there appears to be a hint of correlated residuals in the later epochs from 2014 to 2022 in R.A. (Figure 9).

Additional observations in the future can establish the unlensed source proper motion and confirm or reject any potential discrepancy.

C.3. Bias-corrected Photometric Time Series

Figure 18 compares the HST photometry of OB110462 derived by Sahu et al. (2022; their Figure 13), Lam et al. (2022b; their Figures 7 and 8), and this work. The calibration of the photometry across the three data sets slightly differs. To calculate the difference between the zero-point in the photometry of Lam et al. (2022a) and this work as compared to Sahu et al. (2022), we calculate the average magnitude difference between those data sets and the Sahu et al. (2022) photometry for the seven common epochs between 2011 and 2017. Then to put the photometry all onto comparable footing, this constant zero-point difference is subtracted from the photometry in Lam et al. (2022a) and this work.

There are minor differences between the photometry in Lam et al. (2022a, 2022b) and Sahu et al. (2022) in the early (2011–2012) epochs. With the updated bias correction in the photometry we derive in this work, we find the same photometry as measured by Sahu et al. (2022) within the uncertainties.

Although the astrometric bias is the main reason for the updated mass result, Figure 18 illustrates that the photometric

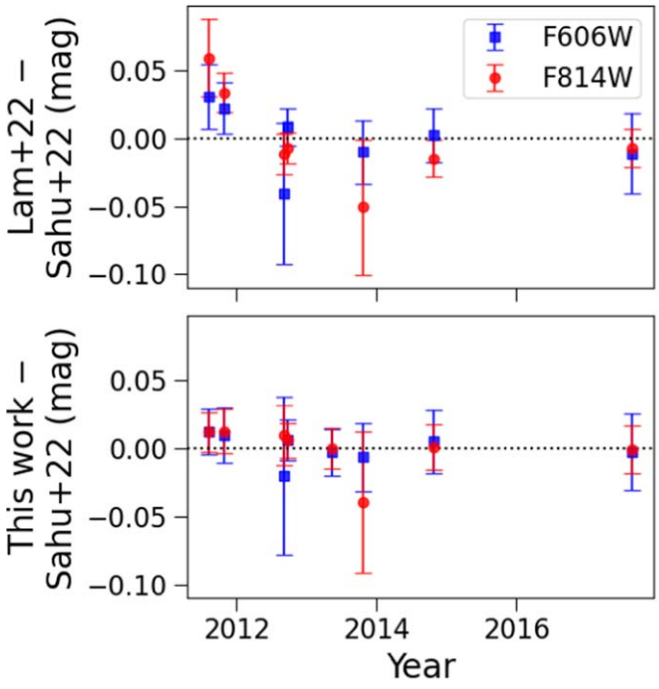

Figure 18. Comparison of HST photometry derived by Lam et al. (2022a, 2022b), Sahu et al. (2022), and this work. The top (bottom) row compares the differences in the photometry in Sahu et al. (2022) to Lam et al. (2022a, 2022b) (this work); red (blue) points denote data in the F814W (F606W) filter.

bias should also not be neglected. In particular, for Roman, with its extremely precise photometry, accounting for such systematics will be important.

ORCID iDs

Casey Y. Lam https://orcid.org/0000-0002-6406-1924
Jessica R. Lu https://orcid.org/0000-0001-9611-0009

References

Anderson, J. 2014, The Impact of x-CTE in the WFC3/UVIS detector on Astrometry, Instrument Science Report, WFC3 2014-02
Anderson, J. 2021, Table-Based CTE Corrections for flt-Format WFC3/UVIS, Instrument Science Report, WFC3 2021-13
Anderson, J. 2022, One-Pass HST Photometry with hst1pass, Instrument Science Report, 2022-5
Anderson, J., Baggett, S., & Kuhn, B. 2021, Updating the WFC3/UVIS CTE model and Mitigation Strategies, Instrument Science Report, 2021-9
Anderson, J., & King, I. R. 2006, PSFs, Photometry, and Astronomy for the ACS/WFC, Instrument Science Report, ACS 2006-01
Anderson, J., Sarajedini, A., Bedin, L. R., et al. 2008, AJ, 135, 2055
Andrews, J. J., & Kalogera, V. 2022, ApJ, 930, 159
Bellini, A., Libralato, M., Bedin, L. R., et al. 2018, ApJ, 853, 86
Chakrabarti, S., Simon, J. D., Craig, P. A., et al. 2023, AJ, 166, 21
Corral-Santana, J. M., Casares, J., Muñoz-Darias, T., et al. 2016, A&A, 587, A61
Dominik, M., & Sahu, K. C. 2000, ApJ, 534, 213
El-Badry, K., Rix, H. W., Quataert, E., et al. 2023a, MNRAS, 518, 1057
El-Badry, K., Rix, H.-W., Cendes, Y., et al. 2023b, MNRAS, 521, 4323
Fender, R. P., Maccarone, T. J., & Heywood, I. 2013, MNRAS, 430, 1538
Hog, E., Novikov, I. D., & Polnarev, A. G. 1995, A&A, 294, 287
Johnson, S. A., Penny, M., Gaudi, B. S., et al. 2020, AJ, 160, 123
Jonker, P. G., Kaur, K., Stone, N., & Torres, M. A. P. 2021, ApJ, 921, 131
Kuhn, B., & Anderson, J. 2021, WFC3/UVIS: New FLC External CTE Monitoring 2009-2020, Instrument Science Report, WFC3 2021-6
Lam, C. Y., Lu, J. R., Hosek, Matthew, W. J., Dawson, W. A., & Golovich, N. R. 2020, ApJ, 889, 31
Lam, C. Y., Lu, J. R., Udalski, A., et al. 2022a, ApJL, 933, L23
Lam, C. Y., Lu, J. R., Udalski, A., et al. 2022b, ApJS, 260, 55
Lu, J. R., Sinukoff, E., Ofek, E. O., Udalski, A., & Kozlowski, S. 2016, ApJ, 830, 41
Mereghetti, S., Sidoli, L., Ponti, G., & Treves, A. 2022, ApJ, 934, 62
Miyamoto, M., & Yoshii, Y. 1995, AJ, 110, 1427
Mróz, P., Udalski, A., & Gould, A. 2022, ApJL, 937, L24
Olejak, A., Belczynski, K., Bulik, T., & Sobolewska, M. 2020, A&A, 638, A94
Özel, F., Psaltis, D., Narayan, R., & McClintock, J. E. 2010, ApJ, 725, 1918
Penny, M. T., Gaudi, B. S., Kerins, E., et al. 2019, ApJS, 241, 3
Sabbi, E., Lennon, D. J., Anderson, J., et al. 2016, ApJS, 222, 11
Sahu, K. C., Anderson, J., Casertano, S., et al. 2022, ApJ, 933, 83
Sana, H., de Mink, S. E., de Koter, A., et al. 2012, Sci, 337, 444
Spergel, D., Gehrels, N., Baltay, C., et al. 2015, arXiv:1503.03757
Thompson, T. A., Kochanek, C. S., Stanek, K. Z., et al. 2019, Sci, 366, 637
Vigna-Gómez, A., & Ramirez-Ruiz, E. 2023, ApJL, 946, L2
Walker, M. A. 1995, ApJ, 453, 37
Wiktorowicz, G., Wyrzykowski, L., & Chruslinska, M. 2019, ApJ, 885, 1